2020-12

A DETERMINISTIC APPROACH TO UNDERSTANDING THE SENSITIVITY OF SURFACE DUCT PROPAGATION TO SOUND SPEED FEATURES IN THE UPPER OCEAN

Zinicola-Lapin, William N.

Monterey, CA; Naval Postgraduate School

NAVAL POSTGRADUATE SCHOOL

MONTEREY, CALIFORNIA

THESIS

A DETERMINISTIC APPROACH TO UNDERSTANDING THE SENSITIVITY OF SURFACE DUCT PROPAGATION TO SOUND SPEED FEATURES IN THE UPPER OCEAN

by

William N. Zinicola-Lapin

December 2020

Thesis Advisor: John A. Colosi
Second Reader: Davis B. Reeder

THIS PAGE INTENTIONALLY LEFT BLANK

REPORT DOCUMENTATION PAGE	*Form Approved OMB No. 0704-0188*

1. AGENCY USE ONLY *(Leave blank)*	**2. REPORT DATE** December 2020	**3. REPORT TYPE AND DATES COVERED** Master's thesis

4. TITLE AND SUBTITLE
A DETERMINISTIC APPROACH TO UNDERSTANDING THE SENSITIVITY OF SURFACE DUCT PROPAGATION TO SOUND SPEED FEATURES IN THE UPPER OCEAN

5. FUNDING NUMBERS

6. AUTHOR(S) William N. Zinicola-Lapin

7. PERFORMING ORGANIZATION NAME(S) AND ADDRESS(ES)
Naval Postgraduate School
Monterey, CA 93943-5000

8. PERFORMING ORGANIZATION REPORT NUMBER

9. SPONSORING / MONITORING AGENCY NAME(S) AND ADDRESS(ES)
N/A

10. SPONSORING / MONITORING AGENCY REPORT NUMBER

11. SUPPLEMENTARY NOTES The views expressed in this thesis are those of the author and do not reflect the official policy or position of the Department of Defense or the U.S. Government.

12a. DISTRIBUTION / AVAILABILITY STATEMENT
Approved for public release. Distribution is unlimited.

12b. DISTRIBUTION CODE
A

13. ABSTRACT (maximum 200 words)

A key sound speed feature of the upper ocean is the Mixed Layer Acoustic Duct (MLAD). Acoustic propagation effects due to mean properties of the duct and spatial and temporal variability are thought to be strong functions of acoustic frequency. Key physical mechanisms at work are diffractive leakage and mode coupling. Using both analytic theory and direct numerical simulation, this thesis will examine 400 and 1000 Hz MLAD propagation characteristics by calculating the sensitivity of duct propagation to various ocean perturbations with horizontal scales ranging from 0.5 to 15 km. As a starting point, sound speed profiles (SSP) typical of the spring-summer transition in the North Atlantic are considered. Tools used are first-order mode scattering theory originally developed for shallow water propagation, and direct numerical simulation. Numerical simulations are compared to theory with the goals of 1) evaluating the utility of the shallow water analytic approach for deep water MLADs and 2) putting forward a metric for estimating MLAD stability as a function of frequency and perturbation scales. Results show that while the shallow water analytic approach is not accurate enough for the MLAD due to higher order mode interaction, first-order mode energy equation motivates the non-dimensional interaction matrix, Γmn, which showed strong correlation between multiple scattering events and increased acoustic variability when $\Gamma mn > 1$.

14. SUBJECT TERMS
acoustic, coupled modes, mixed layer duct, internal waves, interaction parameter

15. NUMBER OF PAGES
77

16. PRICE CODE

17. SECURITY CLASSIFICATION OF REPORT	**18. SECURITY CLASSIFICATION OF THIS PAGE**	**19. SECURITY CLASSIFICATION OF ABSTRACT**	**20. LIMITATION OF ABSTRACT**
Unclassified	Unclassified	Unclassified	UU

NSN 7540-01-280-5500

Standard Form 298 (Rev. 2-89)
Prescribed by ANSI Std. 239-18

THIS PAGE INTENTIONALLY LEFT BLANK

Approved for public release. Distribution is unlimited.

A DETERMINISTIC APPROACH TO UNDERSTANDING THE SENSITIVITY OF SURFACE DUCT PROPAGATION TO SOUND SPEED FEATURES IN THE UPPER OCEAN

William N. Zinicola-Lapin
Lieutenant Commander, United States Navy
BS, University of North Carolina at Wilmington, 2006
MS, North Carolina State University, 2009

Submitted in partial fulfillment of the
requirements for the degree of

MASTER OF SCIENCE IN METEOROLOGY AND PHYSICAL OCEANOGRAPHY

from the

NAVAL POSTGRADUATE SCHOOL
December 2020

Approved by: John A. Colosi
Advisor

Davis B. Reeder
Second Reader

Peter C. Chu
Chair, Department of Oceanography

THIS PAGE INTENTIONALLY LEFT BLANK

ABSTRACT

A key sound speed feature of the upper ocean is the Mixed Layer Acoustic Duct (MLAD). Acoustic propagation effects due to mean properties of the duct and spatial and temporal variability are thought to be strong functions of acoustic frequency. Key physical mechanisms at work are diffractive leakage and mode coupling. Using both analytic theory and direct numerical simulation, this thesis will examine 400 and 1000 Hz MLAD propagation characteristics by calculating the sensitivity of duct propagation to various ocean perturbations with horizontal scales ranging from 0.5 to 15 km. As a starting point, sound speed profiles (SSP) typical of the spring-summer transition in the North Atlantic are considered. Tools used are first-order mode scattering theory originally developed for shallow water propagation, and direct numerical simulation. Numerical simulations are compared to theory with the goals of 1) evaluating the utility of the shallow water analytic approach for deep water MLADs and 2) putting forward a metric for estimating MLAD stability as a function of frequency and perturbation scales. Results show that while the shallow water analytic approach is not accurate enough for the MLAD due to higher order mode interaction, first-order mode energy equation motivates the non-dimensional interaction matrix, Γmn, which showed strong correlation between multiple scattering events and increased acoustic variability when $\Gamma mn > 1$.

THIS PAGE INTENTIONALLY LEFT BLANK

TABLE OF CONTENTS

THIS PAGE INTENTIONALLY LEFT BLANK

LIST OF FIGURES

THIS PAGE INTENTIONALLY LEFT BLANK

LIST OF TABLES

THIS PAGE INTENTIONALLY LEFT BLANK

LIST OF ACRONYMS AND ABBREVIATIONS

CTD	Conductivity, Temperature, and Depth
CZ	Convergence Zone
DSC	Deep Sound Channel
DSCA	Deep Sound Channel Axis
GIUK	Greenland, Iceland, United Kingdom
ML	Mixed Layer
MLAD	Mixed Layer Acoustic Duct
MLD	Mixed Layer Depth
NISKINe	Near-Inertial Shear and Kinetic Energy in the North Atlantic experiment
RP	Reference Publication
SLD	Sonic Layer Depth
SSC	Secondary Sound Channel
SSP	Sound Speed Profile
TL	Transmission Loss

THIS PAGE INTENTIONALLY LEFT BLANK

I. INTRODUCTION

Acoustic propagation within oceanic wave guides is thought to be a strong function of acoustic frequency due to trapping and diffractive effects. Furthermore, the physical properties of these ducts are affected by ocean physics varying in space and time thus leading to scattering processes which are also thought to be strong functions of frequency (Colosi, 2016). The interplay of these effects raises interesting questions regarding ocean duct propagation. Namely high frequencies are effectively trapped by ocean waveguides and suffer little diffractive loss, however, they are more strongly scattered by ocean variability. Low frequencies, on the other hand, are thought to suffer less scattering loss but are not as effectively trapped in waveguides and therefore suffer more diffractive loss. This situation suggests that there can be an optimal frequency for the different waveguides that exist in the ocean. This thesis takes a step in answering this question by examining the frequency dependence of scattering by discrete features in the ocean, in particular those in the upper ocean.

The influence of oceanographic features on acoustic propagation within these acoustic ducts have been studied for many decades. In 1950 Eckart and Carhart state:

> If sound of a constant intensity and frequency is transmitted through the sea from one ship and received on another at some fixed distance, the intensity of the signal received from one second to the next will not be constant; it fluctuates, often by a factor of ten. Indeed, the presence of fluctuation is perhaps the most constant characteristic of sound in the sea!

The field languished for several decades because of inadequate knowledge of real ocean processes. This situation was rectified in the early 70's with the beginning of the mesoscale revolution and the introduction of the Garrett-Munk internal wave spectrum. The field really landed on its feet with the publication of the monograph "Sound propagation through the fluctuating ocean" (Flatte 1979 et al.). The Flatte monograph focused on ray-like methods but simultaneously Dozier and Tappert (1978) took a mode approach and described how random internal waves, can lead to energy exchange between acoustic modes, a process called mode coupling. Specifically, they noted a resonance associated with ocean structure that matched normal mode beat wavenumbers. This beat

wavenumber resonance can give rise to enormous fluctuations in acoustic intensity if the beat wavenumbers at a given acoustic frequency match the energetic scales of sound speed variability in the ocean. For example, Baxter and Orr (1982) showed that at high frequencies the intensity of the sound field could vary by up to 20 dB when interacting with internal waves. Zhou, Zhang, and Rogers (1991) report that these variations are a strong function of time, propagation direction, and frequency. Similar to Dozier and Tappert, Zhou et al. found a "resonance-like" function of packet length and soliton wavelength specifically for shallow water internal wave packets in coastal zones. Building on previous work, a multitude of theoretical and experimental research have been performed to explore the effects of internal waves on acoustic propagation. Tielbuerger, Finette, and Wolf (1997) looked at the acoustic propagation through internal wave fields in shallow water. Finette et al. (2000) looked at the effects due to time varying wave fields. Preisig and Duda (1997) modeled solitary internal waves as a square wave in attempts to shed light on the coupling details and Colosi (2008) expanded on this modeling them as gaussian solitons.

To examine more closely how sensitive acoustic propagation is to oceanographic feature scales, Colosi (2008) took an analytic approach to relate how the spatial scales of oceanographic features directly affect mode coupling. He accomplished this by expanding the scattering matrix via a Dyson series and taking only the first order terms which represent single scattering events. This approach shows that the energy exchange between mode n with mode m is directly related to the width of the perturbation (Δ), depth structure of the perturbation (Z_{mn}), and the beat wavenumber between the modes denoted as

$$k_{mn} = k_n - k_m. \qquad \text{Equation 1}$$

Moreover, it is shown that for small and large Δ the energy exchange is close to zero, revealing the existence of an optimal Δ or ocean feature size of maximum interaction, reinforcing the "resonance-like" conditions previously documented.

This thesis will be expanding the analytical approach taken by Colosi (2008) into deeper water, focusing on the sensitivity of surface duct propagation to spatially varying

oceanographic features, denoted as perturbations. Here we use both the analytic theory and direct numerical simulation for validation. The focus is on upper ocean propagation through sound speed profiles typical of the spring-summer transition in the Eastern North Atlantic. The theory, originally derived for shallow water propagation through sound speed perturbations caused by internal solitary wave packets, will be modified for deep water and perturbations typical of the upper ocean and mixed layer. Numerical simulations will be compared to theory for an assortment of perturbation fields between 0.5 and 15 km at acoustic frequencies of 400 Hz and 1000 Hz.

The questions we will explore are as follows:

1. Can the analytic approach which proved successful in shallow water be expanded to deeper water with similar results?

2. Can we use this expanded analytic approach from Colosi (2008) to provide an understanding of the stability of propagation to perturbations particularly Transmission Loss (TL) effects such as duct leakage, ensonification of shadow zones, and scattering processes?

THIS PAGE INTENTIONALLY LEFT BLANK

II. METHODS

Here we discuss the methods adopted in this research. We will first describe the type of oceanic environment to be studied which is a tactically relevant region of the N. Atlantic south of Iceland. Next our acoustic propagation methods will be described. Here we use the method of normal modes which identifies ducted and non-ducted acoustic energy. The normal mode approach will be used in two ways,

1) To carry out reduced physics computations, via the Dyson series, to predict the sensitivity of mode coupling to the spatial scales of various ocean features and

2) To perform full physics direct numerical simulation of sound propagation.

A. ENVIRONMENT

The lack of research on coupled mode theory and resonance conditions in the upper ocean of deep-water environments, as well as the tactical relevance inspired us to focus on the N. Atlantic near the mid-Atlantic Ridge (Figure 1). Here we took advantage of an extensive oceanographic experiment carried out during the 2019 May–June time frame called the Near-Inertial Shear and Kinetic Energy in the North Atlantic experiment (NISKINe). Though they were not explicitly focused on acoustic propagation, they did carry out six full water column conductivity, temperature, and depth (CTD) profiles sampling the thermohaline structure across a warm core eddy every 20 km (Figure 2).

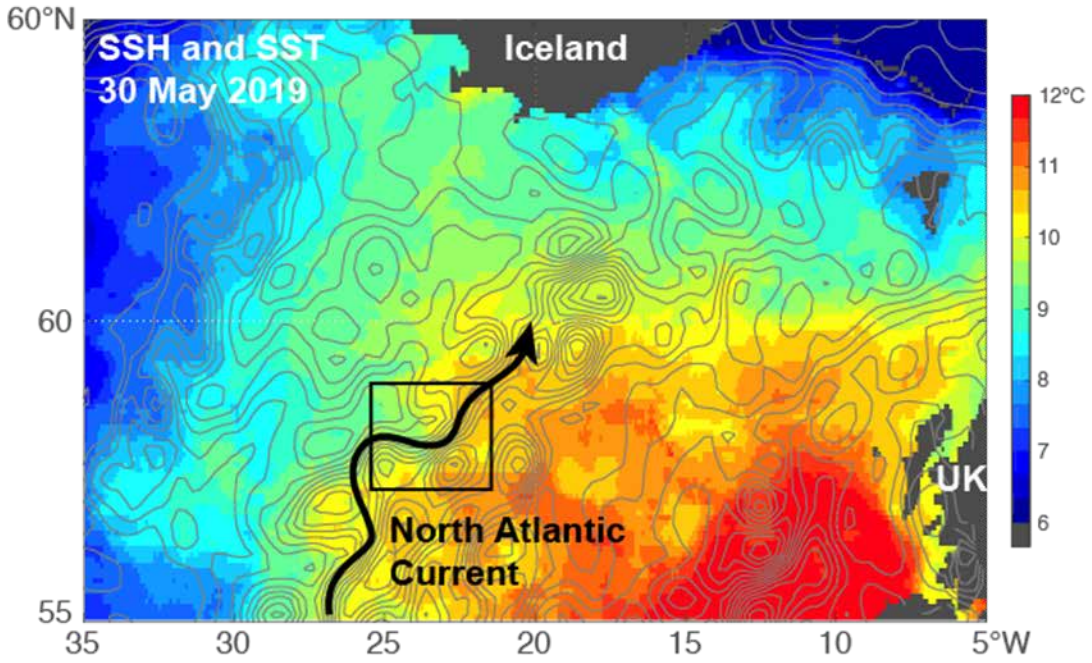

Figure 1. Map of sea surface temperature from passive microwave and sea surface height (Aviso, near-real-time) at the end of May. The black box shows the region where the cruise took place. Source: Rainville, and Coauthors (2019).

The CTDs are numbered 1–6 and their locations are denoted by the solid black lines in Figure 2. CTD 1 is on the far right outside of the eddy and CTD 6 is on the far left inside the eddy. Each CTD contained a downcast and upcast collected as the sensor was deployed to depth and then retrieved back up to the ship. Only the downcast data was used to generate the sound speed profiles (SSP) in our research because the CTD instruments are positioned on the underside of the CTD cage and therefore the down cast has the measurements carried out with undisturbed water.

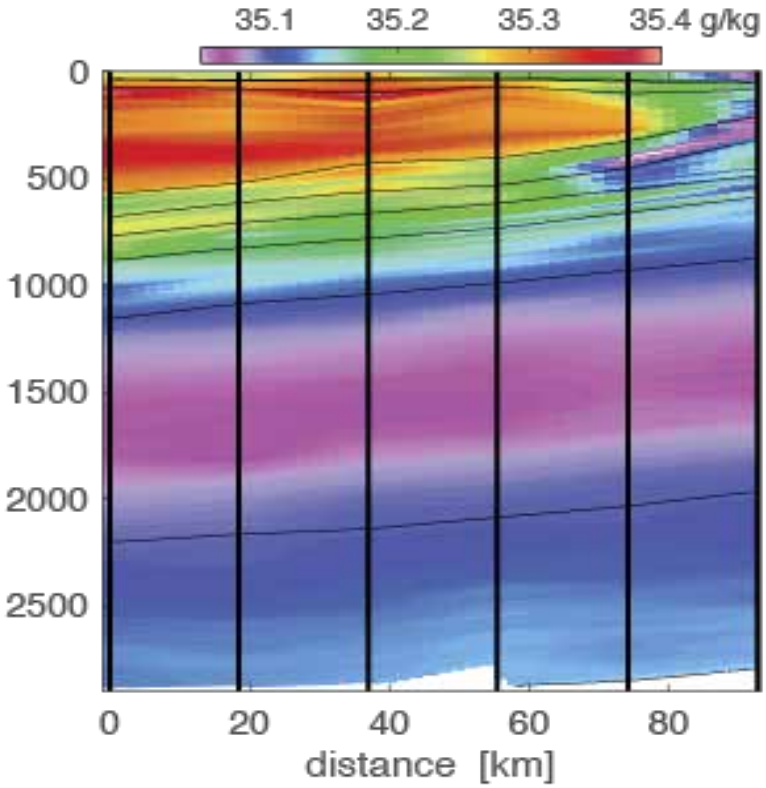

Figure 2. Absolute salinity versus depth and distance (from the station closest to the center of anticyclone, here positive moving north) for the hydrographic section. Station locations are indicated by the thick black lines with CDT1 on the far right and CDT6 on the far left. Potential density contours are plotted (0.1 kg m-3 intervals). Source: Rainville, and Coauthors (2019).

We converted the CTD data into SSPs via the sea water toolbox, seawater ver3 3.1, found at http://www.cmar.csiro.au/datacentre/ext_docs/seawater.htm, with a reference latitude of 58 degrees North, roughly the midpoint for all CTDs. The latitude is required for the pressure to depth relationship of Earth's gravitational field changes slightly with latitude. In this work each profile is treated independently, that is we will not be concerned with propagation through the range dependent set of profiles as the section is too sparse. Of great interest, but not part of this thesis due to time constraints, is the sensitivity of the propagation and scattering to the background sound speed profile since this profile sets the beat wavenumbers. In this work we focused only on CTD 1. The raw SSPs were linearly interpolated onto a uniform depth grid with 1 m spacing and then smoothed removing all

variability with vertical wavelengths less than 100 m. This smoothing removes mostly internal wave effects and thus gave us a large-scale view of SSPs typical for the N. Atlantic during the transition period of May–June. Each SSP is plotted in Figure 3 compared to climatological average for the month of June where we see significant variation from the climatology in both the deep sound channel and the secondary (shallower) duct.

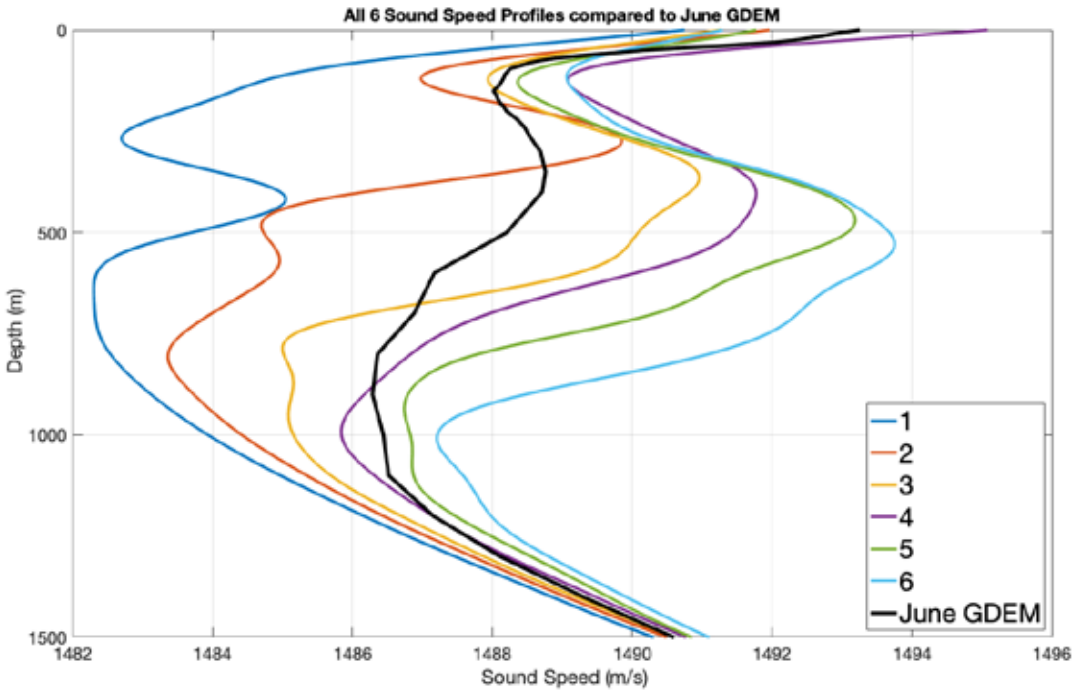

Figure 3. All six smoothed SSPs compared to June GDEM climatology (solid black)

As previously mentioned, we chose to use SSP1 derived from CTD1 for all of our acoustic analysis in this thesis because it is outside the eddy. An interesting follow up study could look at the effects of the eddy on scattering in and out of the surface duct.

Comparing SSP1 to the climatological SSP for the time period and location (Figure 3), we find that the strong secondary sound channel (SSC) is not unique to the NISKINe experiment but is a common feature in the water space for the season and location. In addition, we see the lack of a prominent mixed layer (ML) in our SSPs match nicely with

the climatology. This is not too surprising because it is common for the upper ocean to re-stratify during the transition months. This re-stratification leads to a shallower ML and corresponding shallower sonic layer depth (SLD). Figure 4 shows the climatological SSPs for each month of the year. We can see that the ML feature for this location in the N. Atlantic does not begin to form until September but extends quite deep in the winter months due to the wind forcing of frequent storms and surface cooling. A maximum ML depth or MLD of approximately 450 m is seen in March. The ML begins to re-stratify in April and the SSC becomes the predominate upper ocean feature sometime during the first ordermode timeframe.

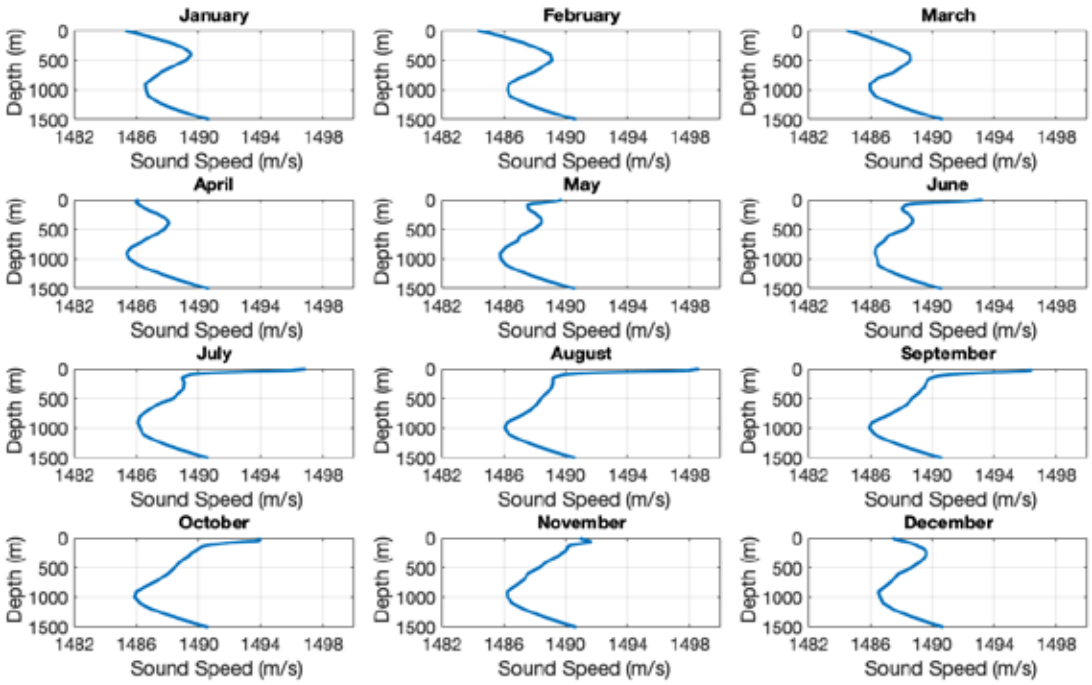

Figure 4. SSPs derived from GDEM Climatological data for every month of the year, location 57N, 24W. Note, that the water depth is much deeper, figures are only showing first 1500 m to better display the upper ocean structure.

Climatology data from ARGO floats are shown in Figure 5 where the MLDs in the month of May have an average value of approximately 80 meters +/- 50 meters and then jump to 25 meters +/- 10 meters in June as the re-stratification takes place. Since the

NISKINe CTDs were taken early in the month of June, we decided to add a ML to SSP1 of 70 m with a constant sound speed gradient of 0.026 s^{-1}. The updated SSP1 with the additional ML can be seen in Figure 6. The 70 m ML supports only one trapped mode at 400 Hz and three trapped modes at 1000 Hz (Equation 2) allowing us to more readily identify mode coupling interactions between trapped modes and untrapped modes. The original SSC supported many trapped modes (Equation 3 and Figure 9) making the initial analysis complicated and too complex to identify primary interactions. ML cutoff frequencies and trapped modes for SSP1 are described in detail below.

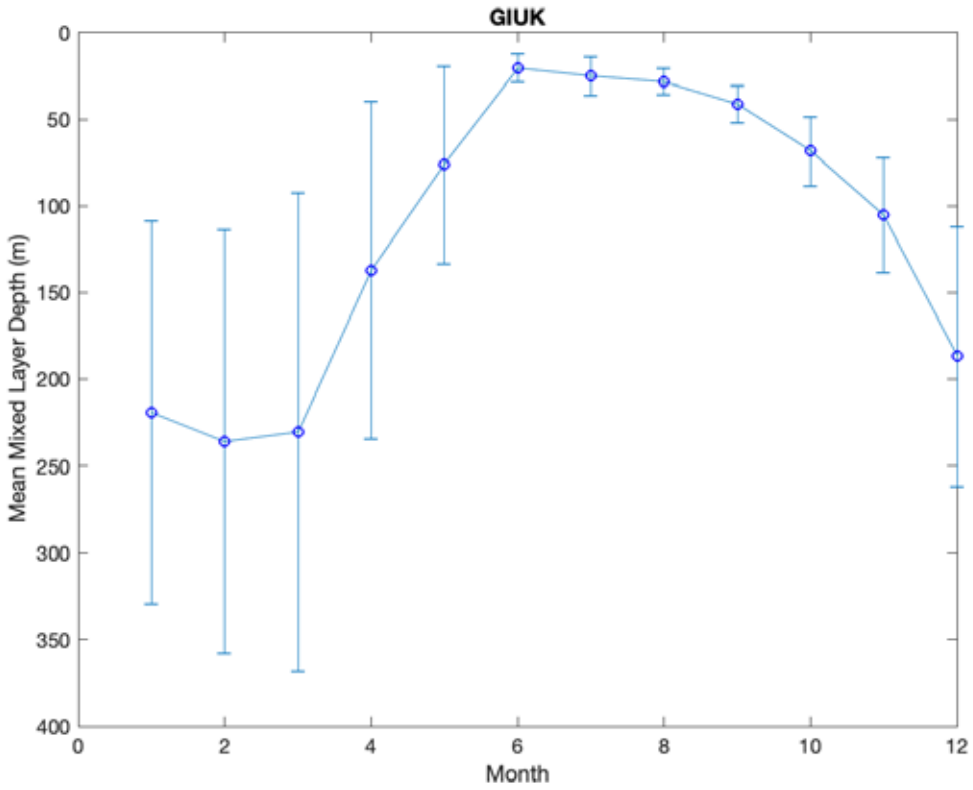

Figure 5. ARGO Float MLD climatology values for water space near the Greenland, Iceland, United Kingdom (GIUK) gap for all months of the year including the average deviation from the mean value.

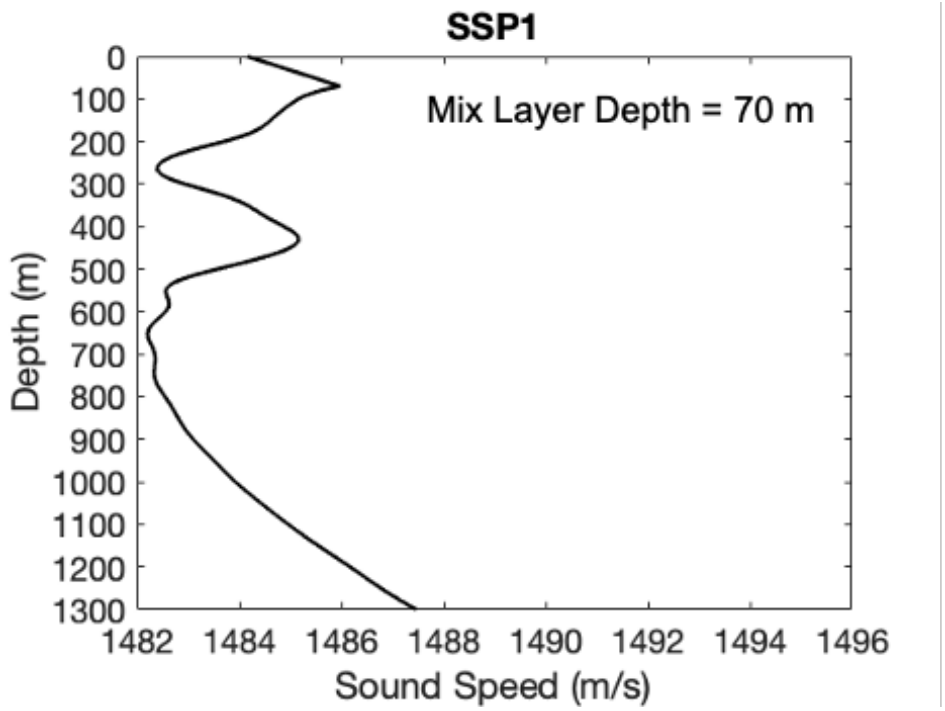

Figure 6. SSP1 with a ML of 70 m added to the profile to match the climatology constant with the transition period of the May–June timeframe.

Before preceding further, a brief overview of common upper oceanographic regions is needed. Due to wind forcing and vertical heat flux from the surface, the upper portion of the ocean almost always consists of some kind of a ML. The depth of this ML, called the MLD, varies in time (hours, days), season, distance, and geographical location. With roughly uniform temperature and salinity in the ML, the sound speed increases linearly with an adiabatic gradient of 0.016 s^{-1} to a subsurface maximum which is denoted as the Sonic Layer Depth (SLD). The SLD and MLD tend to be very close in value to each other, and like the MLD, the SLD varies as well, typically being deeper in the winter and shallower in the summer. This increase in sound speed with depth creates an acoustic duct called the Mixed Layer Acoustic Duct (MLAD) (Colosi et. al. 2020). As seen in Equation 2 from Urick (1982) the number of modes "n" that can be trapped in the MLAD depends on the SLD denoted as "h," the sound speed gradient within the ML $\left(\frac{dc}{dz}\right)_{ML}$, and the average sound speed $c_o \approx 1500\ {}^{m}/_{s}$.

$$f_{min}(n) = \frac{3(4n-1)}{16}\sqrt{\frac{c_o^3}{2h^3}\left(\frac{dc}{dz}\right)^{-1}_{ML}}.$$ Equation 2

Strongly trapped sound, $f \gg f_{min}$ experiences much less energy loss with propagation and will propagate great distances if the duct holds. For SSP1 with a SLD matching the MLD of 70 m, the cutoff frequency for n = 1 mode through 4 modes is 244.7 Hz, 570.9 Hz, 897.2 Hz, and 1223.4 Hz, respectively. Therefore, using a frequency of 400 Hz and 1000 Hz, we expect to see one trapped mode at 400 Hz and three trapped modes at 1000 Hz. The trapped modes for each frequency are shown in Figure 7.

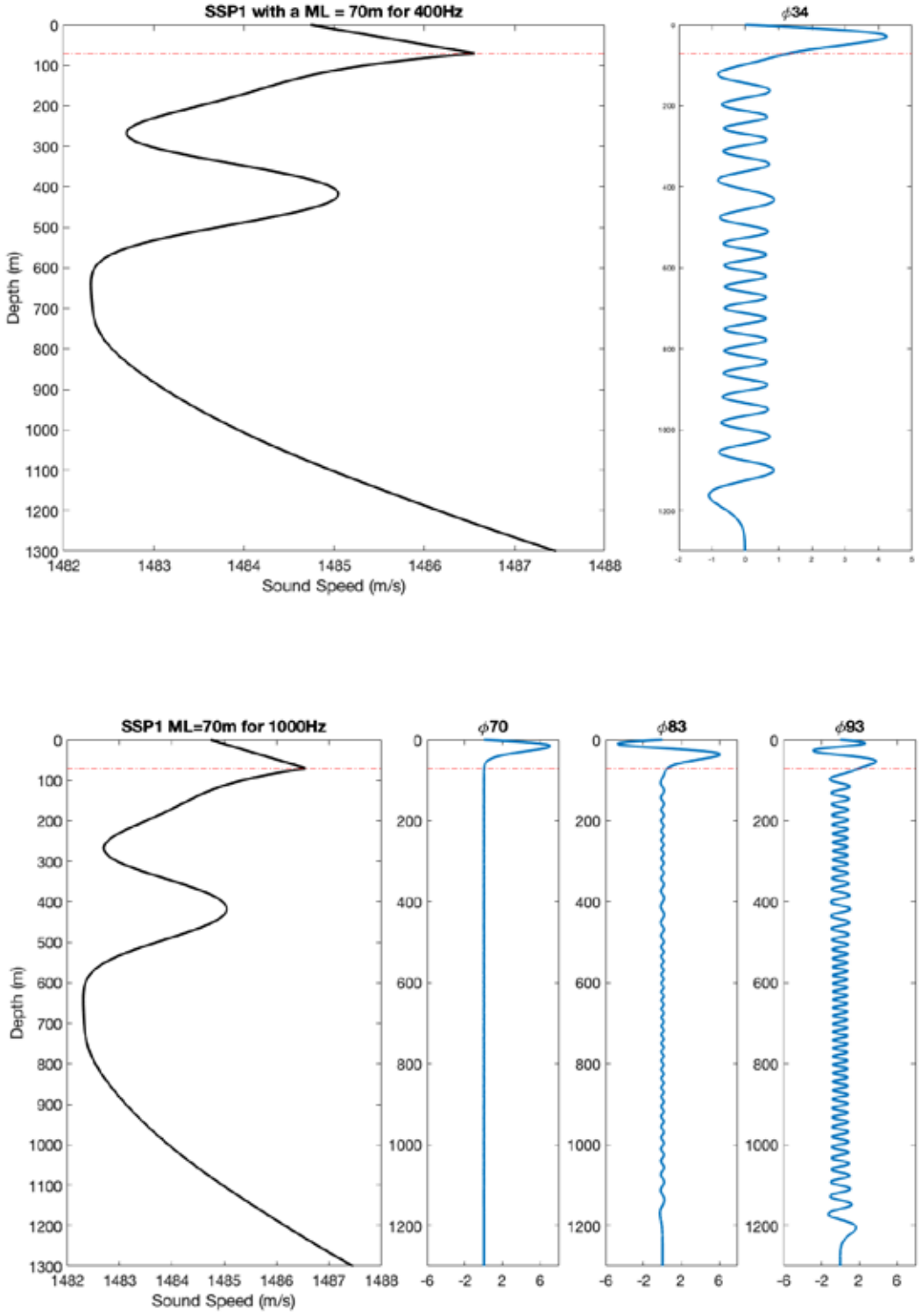

Figure 7. Displays ML mode 1 (mode 34) for SSP1 at 400 Hz and ML mode 1, 2, 3 (modes 70, 83, 93) at 1000 Hz for a MLD of 70 m denoted by the horizontal line.

At 400 Hz, mode 34 (ML mode 1) is trapped but has significant energy below the MLD implying diffraction of acoustic energy into the water column below. At 1000 Hz we see that modes 83 (ML mode 2) and 93 (ML mode 3) are similar to mode 34 at 400 Hz with energy below the duct. However, at 1000 Hz mode 70 (ML mode 1) is very strongly trapped with very little energy leaking into the deeper water column. This also means that this mode 1 will not feel any of the sound speed perturbations below the duct.

Below the ML, the temperature decreases rapidly with depth. This region is known as the transition layer and it varies in thickness from a few tens of meters to a few hundreds of meters. Below the transition layer is the main thermocline easily identified by its larger negative vertical temperature gradient. The thermohaline structure in the N. Atlantic near this site is unusual because of the existence of a thermopause in the thermocline; this is a region of weak or even sometimes reversed temperature gradient. The vertical temperature gradient below the main thermocline is much less than in the main thermocline and is close to the adiabatic gradient. Therefore, temperature variations tend to be small beneath the main thermocline. Pressure in this deeper region dominates the SSP. Consequently, sound speed will typically decrease with depth in the main thermocline then begin to increase again as the vertical pressure gradient term dominates. The switch from decreasing sound speed to increasing sound speed creates what is known as a deep sound channel (DSC) with the sound speed minimum found at the deep sound channel axis (DSCA). Similar to the MLAD, the DSC will also trap sound with certain frequencies.

If conditions are just right one can have a SSC in the upper ocean. The Fleet Oceanographic and Acoustic Reference Manual (RP 33) states that “SSCs occur in the upper levels of the water column in the thermocline, within and below the surface layer.” The RP 33 also states that “to be considered useful, a SSC must be within the depth capabilities of the applicable tactical sensor, its thickness must be at least 100 feet (30.48 meters), and its strength $\Delta c = c_b - c_{axis}$ must be at least 2.5 ft/s (0.762 m/s).” Figure 8, taken from the RP 33, describes these features in detail.

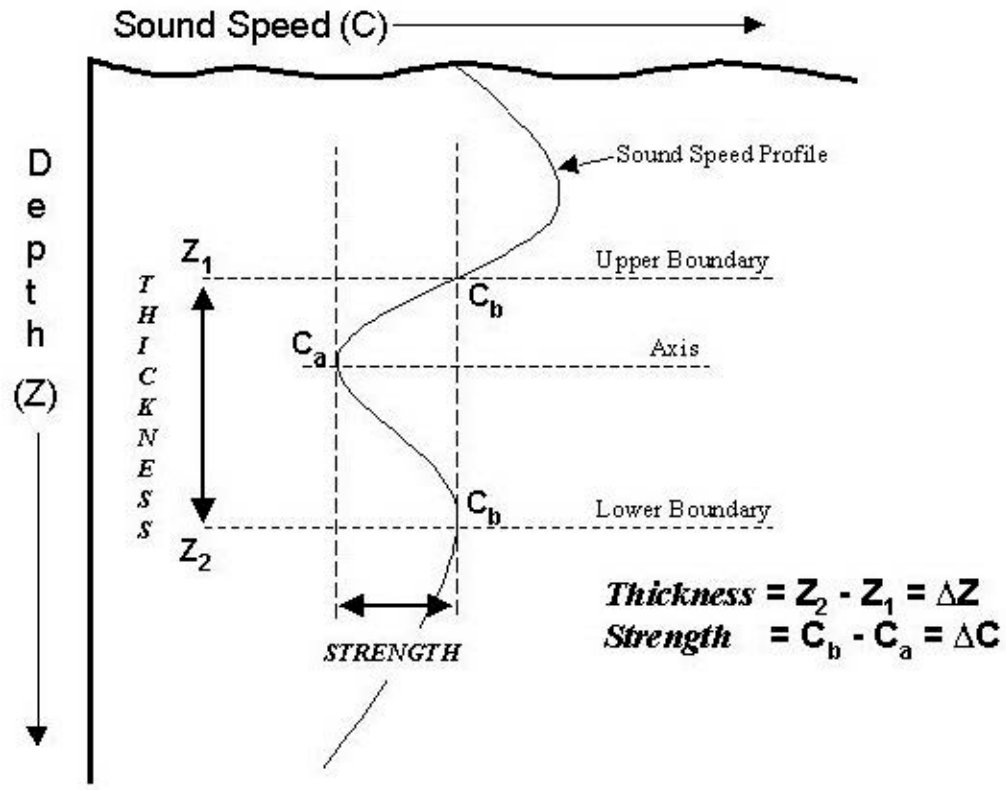

Figure 8. Description of SSC features. Source: Naval Oceanographic Office (1986).

As stated earlier, SSCs are found in the NISKINe profiles (Figure 3). It is common for the upper ocean to re-stratify during the transition months leading to a much shallower SLDs and in some cases very little SLD exists at all. Based on the climatological SSPs shown in Figure 4 for the N. Atlantic, it is apparent that re-stratification happens quickly here eliminating the ML and corresponding MLD and SLD almost completely. Also, we see that in the SSPs derived from the NISKINe data collected in early June (Figure 3) lack a prominent SLD and therefore very little. For reasons stated above we decided to manually create a shallow ML by inserting a 70 m MLD and generating a MLAD above the SSC and DSC.

The SSC in SSP1 will trap sound of a given frequency similar to the MLAD allowing for extended acoustic range propagation. As with all acoustic ducts and or sound channels, diffractive and scattering interactions between these sound speed features can

lead to energy exchange between acoustic ducts and modes. This energy exchange is a strong function of frequency, sound speed gradient, and thickness of the ducts. Equation 3 is the cutoff frequency for the n[th] trapped mode in a SSC. Here c_{axis} is the sound speed at the SSC axis, $\Delta C = c_b - c_{axis}$ also known as the strength of the duct, c_b is the sound speed at the boundary of the SSC, and ΔZ is the vertical channel thickness in meters.

$$f_{\min} = \frac{3}{2}\left(\sqrt{\frac{c_{axis}^3}{8\Delta C}}\right)\left(\frac{1}{\Delta Z}\right)\left(n - \frac{1}{2}\right). \qquad \text{Equation 3}$$

The mode cutoff frequencies for the original SSC of SSP1 at 400 and 1000 Hz are shown in Figure 9.

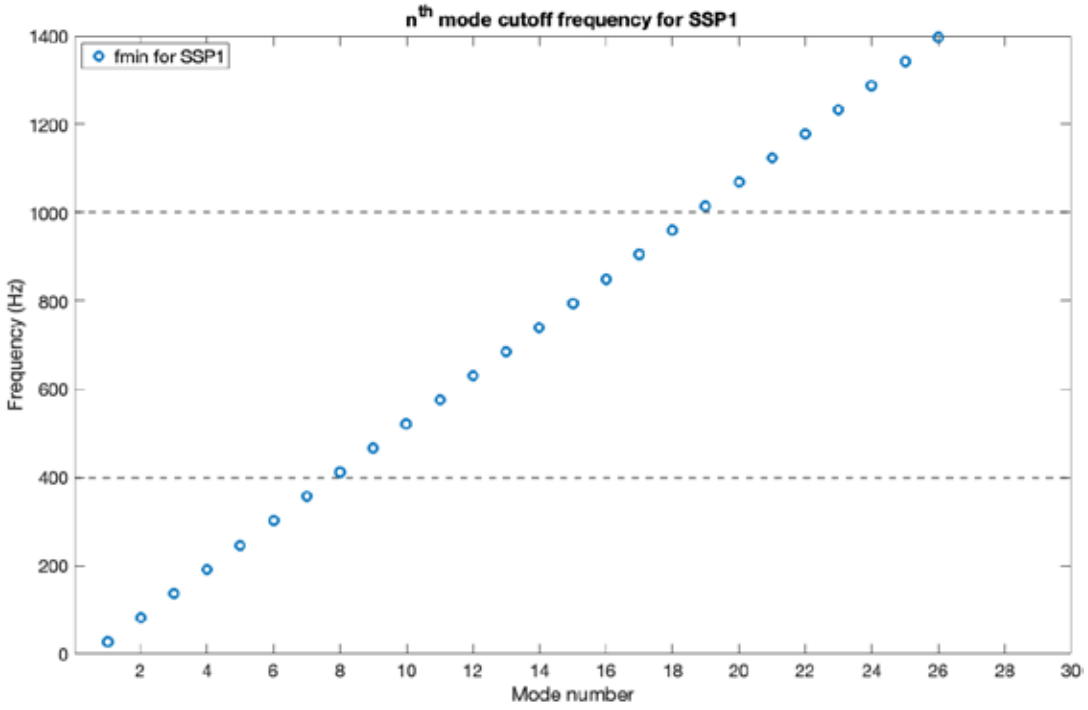

Figure 9. Cutoff frequency for the n[th] mode for SSP1.

At 400 Hz we have 7–8 trapped modes within the SSC and at 1000 Hz we expect almost 20 trapped modes. This many highly energetic trapped modes scattering energy in

and out of the SSC is far too many modes to track. By inserting a MLD/SLD of 70 m creating a MLAD above the SSC that only supports 1 mode at 400 Hz and 3 modes at 1000 Hz yielded a system where disentangling the core physics of energy coupling became much more manageable.

The bulk of the research below focuses on the sensitivity of this energy exchange between the MLAD, the SSC, and the DSC for SSP1 at frequencies of 400 and 1000 Hz to various oceanographic feature sizes commonly found in this region.

B. AN ACOUSTIC EXAMPLE IN THE NORTH PACIFIC

We pause here to discuss samples of transmission loss (TL) due to perturbation scales in the Eastern Pacific taken in the spring of 2005. Figure 10 consists of two separate images. The image on the bottom is an idealistic ocean environment with a range independent sound speed profile and MLD denoted by the solid black line. For a 400 Hz source at 40 m depth we see the TL represented by the various colors with values corresponding to the color bar on the right. In this idealistic case we have a robust MLAD with strong signal out to about 50 km, picking up again in the middle due to the constructive interference of prominent acoustic modes trapped within the MLAD, and repeated convergence zone (CZ) signal every 50 km out to 200+ km. Also, below the ML and in the first 50 km we see a shadow zone that is significantly ensonified by the diffractive tail of ML mode 1.

The upper image in Figure 10 is the range dependent ocean environment taken from high resolution CTD data. We can see the variations in the MLD are nonuniform in both depth and range. These types of perturbations are modeled by Δ, the horizontal distance parameter, and Z_{mn}, the depth dependent matrix in this thesis. A non-dimensional metric to quantify the strength of acoustic sensitivity to both horizontal and vertical spatial scales is described by what we define as Γ_{mn}, the interaction parameter, in the sections below. These parameters will be described in depth later and are only introduced here to emphasize the analogy and comparison between the N. Pacific TL images and the N. Atlantic case.

The effects of sound speed perturbations are clearly seen in this side-by-side comparison. The shadow zone in the bottom idealistic case has been ensonified due to

diffractive and scattering interactions. Also, we see the strong ML signal has been greatly reduced, being scattered into CZ paths. The acoustic sensitivities seen in Figure 10 are strong functions of feature size and acoustic frequency and this thesis takes steps to mathematically describe how these sensitivities are coupled specifically for the chosen region in the N. Atlantic.

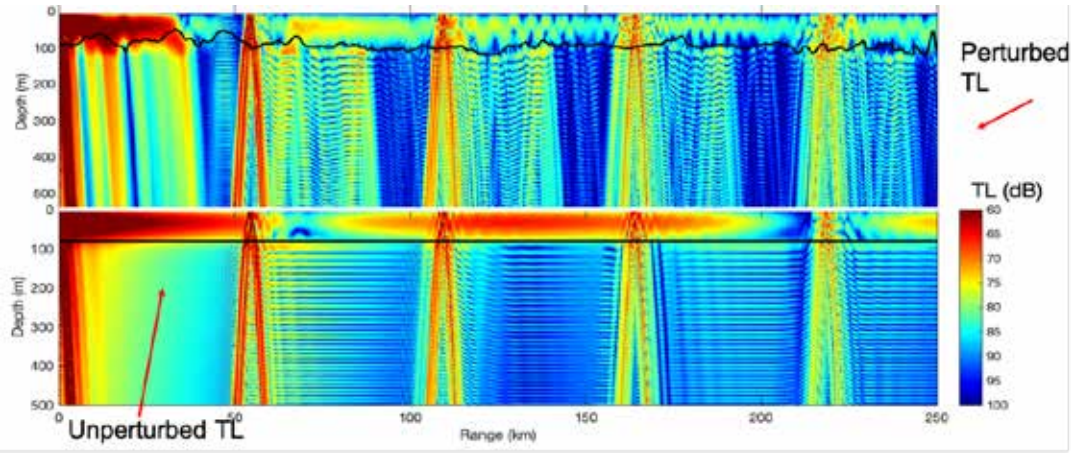

Figure 10. Perturbed (top) and unperturbed (bottom) TL for a 400 Hz frequency source. Source: Colosi and Rudnick (2020).

C. COUPLED MODE THEORY

We considered the smoothed SSP1 to be the unperturbed background sound speed which is independent of range and only a function of depth. The sound speed perturbations ($\delta c(r,z)$) however, will be a function of both depth and range. Therefore, the total sound speed $c_{total}(r,z)$ is

$$c_{total}(r,z) = c(z) + \delta c(r,z). \qquad \text{Equation 4}$$

Using the method of normal modes (Colosi 2016, 2008), we can write the pressure for a given frequency in terms of the normal modes of the background or unperturbed ($\delta c(r,z)$=0) sound speed profiles, that is

$$p(r,z) = \sum_{n=1}^{N} \frac{A_n(r)}{\sqrt{k_n r}} \varphi_n(z) \quad .$$ Equation 5

$A_n(r)$ are the range varying mode amplitude functions which exclusively contain the acoustic variability with range. The vertical eigenmode functions are denoted as φ_n, with eigen wavenumbers k_n satisfying the unperturbed mode equation

$$\sigma(z)\frac{\partial}{\partial z}\left(\frac{1}{\sigma(z)}\frac{\partial \varphi_n}{\partial z}\right) + \left(\bar{k}^2(z) - k_n^2\right)\varphi_n = 0 \quad ,$$ Equation 6

with boundary conditions $\varphi_n(0) = 0$ and the continuity of both pressure and normal velocity at the seafloor interface. Here $\sigma(z)$ is the background unperturbed density function and $\bar{k}(z) = {}^{\omega}/_{c(z)}$.

Following Colosi (2008), Dozier and Tappert (1978a), and Dozier (1983) in the narrow angle weak forward scattering approximation for the Helmholtz equation we can scale the mode amplitude as $\psi_n(r) = A_n e^{-il_n r}$ where $l_n = k_n + i\alpha_n$ is the complex horizontal wavenumber with the $\psi_n(r)$ satisfying the one-way equation

$$\frac{\partial \psi_n}{\partial r} = -i\sum_{m=1}^{N} \rho_{mn}(r) e^{il_{mn}r} \psi_m(r) \quad ,$$ Equation 7

with $l_{mn} = l_m - l_n$. Here $\rho_{mn}(r)$ is the symmetric coupling matrix and is defined as the following.

$$\rho_{mn}(r) = \frac{k_o^2}{\sqrt{(k_m k_n)}} \int_0^{\infty} \mu(r,z) \frac{\varphi_n \varphi_m}{\sigma(z)} dz$$

$$\mu(r,z) = \frac{\delta c(r,z)}{c_o} \quad ,$$ Equation 8

$k_o = {}^{\omega}/_{c_o}$ is the reference wavenumber computed from the given acoustic frequency ω and the reference sound speed c_o which we set at a constant 1500 m/s.

To compare the analytical results to a direct simulation we used the eigenvalue method described in Dozier and Tappert (1978b), which provides a numerical solution to Equation 7. This method closely follows Colosi (2008) but with a source depth of 40 m and a point source frequency simulated at 400 Hz and 1000 Hz.

D. DYSON SERIES SOLUTIONS

Assuming that the mode amplitudes $\psi_n(r)$ can be expanded in a power series of increasing order in a small parameter ϵ associated with the small size of ρ_{mn} then Equation 7 can be solved using the Dyson series as seen in (Colosi 2008, 2016, Dozier and Tappert 1978, Yang 2014, Sakurai 1985). To second order this yields

$$\psi_n(R) = \psi_n(0) - i\sum_{m=1}^{N}\psi_m(0)S_{mn}^{(1)} - \sum_{m=1}^{N}\sum_{j=1}^{N}\psi_j(0)S_{mnj}^{(2)}. \qquad \text{Equation 9}$$

Here $\psi_n(r)$ is the mode amplitude at the receiver which is placed at some range R beyond the perturbation, and $\psi_n(0)$ is the initial amplitude at the source. The first and second order scattering matrices are $S_{mn}^{(1)}$ and $S_{mnj}^{(2)}$. Again, following the notation from Colosi (2008) these scattering matrices are given by the following equations.

$$S_{mn}^{(1)} = \int dk\,\hat{\rho}_{mn}(k)\int_{-\frac{R}{2}}^{\frac{R}{2}} dr' e^{i(l_{mn}-k)r'} \qquad \text{Equation 10}$$

$$S_{mnj}^{(2)} = \int dk \int dk'\,\hat{\rho}_{mn}(k)\hat{\rho}_{jm}(k')\int_{-\frac{R}{2}}^{\frac{R}{2}} dr' \int_{-\frac{R}{2}}^{r'} dr'' e^{i((l_{mn}-k)r' + (l_{jm}-k)r'')}, \qquad \text{Equation 11}$$

with $\hat{\rho}_{mn}(k) = \frac{1}{2\pi}\int_{-\infty}^{\infty} dr\,\rho_{mn}(r)e^{ikr}$ as the Fourier transform of the coupling matrix.

By multiplying Equation 9 with its complex conjugate and dropping terms higher than order two, we obtain an extremely important acoustic observable: the change in modal energy due to coupled mode interaction through the oceanographic perturbation or feature,

$$\left|\psi_n(R)\right|^2 = \left|\psi_n(0)\right|^2 + 2\sum_{m=1}^{N}\psi_m(0)\psi_n(0)\,\mathrm{Im}(S_{mn}^{(1)}) - 2\sum_{m=1}^{N}\sum_{j=1}^{N}\psi_j(0)\psi_n(0)\,\mathrm{Re}(S_{mnj}^{(2)}) + 2\sum_{m=1}^{N}\sum_{j=1}^{N}\psi_m(0)\psi_j(0)S_{mn}^{(1)}(S_{jn}^{(1)})^*$$

Equation 12

The Dyson series physically represents a multiple scattering series where the zeroth-order term has no scattering therefore no mode coupling. The first order term is the single scattering term or one coupling event. The second-order term represents two scatterings or two couplings and so on and so forth. Here we have chosen to show the first order scattering $S_{mn}^{(1)}$ terms and second order scattering terms $S_{mnj}^{(2)}$ only. We will be devoting the rest of the thesis to first order scattering term since its magnitude is a measure of the transition from single to multiple scattering.

E. ACOUSTIC MODEL

A primary goal of this thesis is to shed light on the acoustic sensitivity of a given frequency to common oceanographic features found in the North Atlantic. Following Colosi (2008) we chose to model these oceanographic features as "Gaussian-like" perturbations in both depth and range.

We consider sound speed perturbations generated by ocean processes that give rise to vertical displacements such as eddies or internal waves. The normalized displacement function for this type of model is given by

$$\zeta(r,z) = N_\zeta \zeta_o z \exp\left[-\left(\frac{z}{D_z}\right)^2\right]\exp\left[-\frac{(r-r_o)^2}{\Lambda^2}\right], \qquad N_\zeta = \frac{D_z}{\sqrt{2}}e^{-\frac{1}{2}}$$

Equation 13

Here the gaussian perturbation is centered at $r_o = 30\ km$, $\zeta_o = 40\ m$ is the maximum vertical displacement, $D_z = 200\ m$ is the overall depth of the feature, and Δ is the width of the feature. This form is useful because the Fourier transform of the Gaussian yields another Gaussian.

We now need a relationship between the displacement model and the resulting sound speed perturbations. Since the sound speed is changing rapidly in the upper ocean, we need a nonlinear method to account for sound speed changes due to vertical displacements. Here we use

$$c_p(z+\zeta(r,z)) = c(z)+\gamma_a\zeta(r,z), \quad \text{Equation 14}$$

where c_p is the sound speed of the parcel and γ_a is the adiabatic sound speed gradient (0.016 s^{-1}). This equation says that if we take a parcel at depth z with sound speed $c(z)$ and move it adiabatically to a new depth $z + \zeta(r, z)$, this will be the new parcel sound speed. At this new depth the parcel will be surrounded by fluid with sound speed $c(z + \zeta(r, z))$, therefore the sound speed perturbation will be

$$\delta c(r,z) = c(z+\zeta(r,z)) - c_p(z+\zeta(r,z)). \quad \text{Equation 15}$$

Note that if we Taylor expand the first term in Equation 15, we get the well know results that $dc = \left(\frac{dc}{dz}\right)_p \zeta$. Given a sound speed perturbation in Equation 15 and only considering first order scattering events, Colosi (2008) showed that the total mode energy at a distance R from the source is given by□

$$\left|A_n(R,t)\right|^2 = \left[\left|A_n(0)\right|^2 + 2\sqrt{\pi}\sum_{m=1}^{N} A_m(0)A_n(0)Z_{mn}X_{mn}\sin(k_{mn}r_o(t))\right]e^{-2\alpha_n R}. \quad \text{Equation 16}$$

Once again k_{mn} is the beat wavenumber defined in Equation 1, α_n are the imaginary component of the complex modal wavenumber and represent modal attenuation, the matrix Z_{mn} is the mathematical representation of the mode coupling from the depth structure and is defined as

$$Z_{mn} = -\frac{\omega^2}{c_o^2\sqrt{k_m k_n}}\int_0^\infty \frac{\delta c(z)}{c_o}\frac{\varphi_n(z)\varphi_m(z)}{\rho_o(z)}dz, \quad \text{Equation 17}$$

and X_{mn} represents the contribution to the mode coupling due to the horizontal structure of the feature and is given by

$$X_{mn} = \Lambda \exp\left(\frac{-k_{mn}^2 \Lambda^2}{4}\right). \quad \text{Equation 18}$$

The total mode energy, Equation 16, provides a wealth of insight into the relationship between spatial scales of the oceanographic feature and acoustic mode coupling.

- For small and or large Δ, corresponding to small or large oceanographic features, the X_{mn} is approximately zero meaning there is a limit at both ends of the size spectrum to the energy exchange between the trapped modes. This result suggests the existence of an optimal Δ for maximum energy exchange. Therefore, there will be a range of ocean feature sizes that are acoustically interactive.

- Z_{mn} represents the contribution to mode energy exchange due to the depth structure of the perturbation and the acoustic modes. Non-zero contributions from this term depend on the overlap of $\delta c(z)$ with $\varphi_n(z)$ and $\varphi_n(z)$; therefore Z_{mn} enforces near neighbor coupling.

- For single scatter events the mode coupling is dependent on initial energy of the modes $A_m(0)A_n(0)$.

- We see the existence of the $\sin(\mathrm{k_{mn}r_o(t)})$ term meaning that the coupled mode energy will oscillate as both the perturbation and or source/receiver move in time. This comes about because in first order theory the coupling is dependent on the relative phases of the two modes. In higher order scattering this is not the case and we hypothesize in the real ocean there is no consistent deterministic phase relationship.

Since all the mode coupling interaction is contained within the $Z_{mn}X_{mn}$ terms we define a nondimensional metric to quantify the strength of mode coupling that is,

$$\Gamma_{mn} = \left| 2\sqrt{\pi}(Z_{mn}X_{mn}) \right|. \qquad \text{Equation 19}$$

Γ_{mn}, the interaction parameter, contains all the sensitivity of mode coupling to the spatial scales of oceanographic features and is independent of source and receiver location. We hypothesize that when $\Gamma_{mn} \gg 1$ we have strong mode coupling, many multiple scattering events, and high acoustic sensitivity to feature size. For $\Gamma_{mn} \ll 1$ we will see less acoustic sensitivity to feature size, weaker coupling, and less multiple scattering events.

III. RESULTS

A. 400 HZ SIMULATIONS

1. Correlation between $\Gamma_{mn} \gg 1$ and Multiple Scattering at 400 Hz

The analytic model: At 400 Hz and a source depth of 40 m, there is only one trapped mode, mode 34. So we hypothesize that if there is some n for which Γ_{34n} is of order or greater than 1 we would be in a multple scattering regime in which the TL for mode 34 would have large variability. For this profile at 400 Hz, Figure 11 displays Γ_{34n} for Δ values from 100 m to 50 km. Here we see for various Δ values, several modes interacting with mode 34 that have values of Γ of order or greater than 1. This model shows that for small Δ values (<5 km) mode 34 prefers to couple up into higher mode number and thus higher angle. But as Δ increases (>5 km) mode 34 strongly prefers to couple down with its nearest neighbor, mode 33.

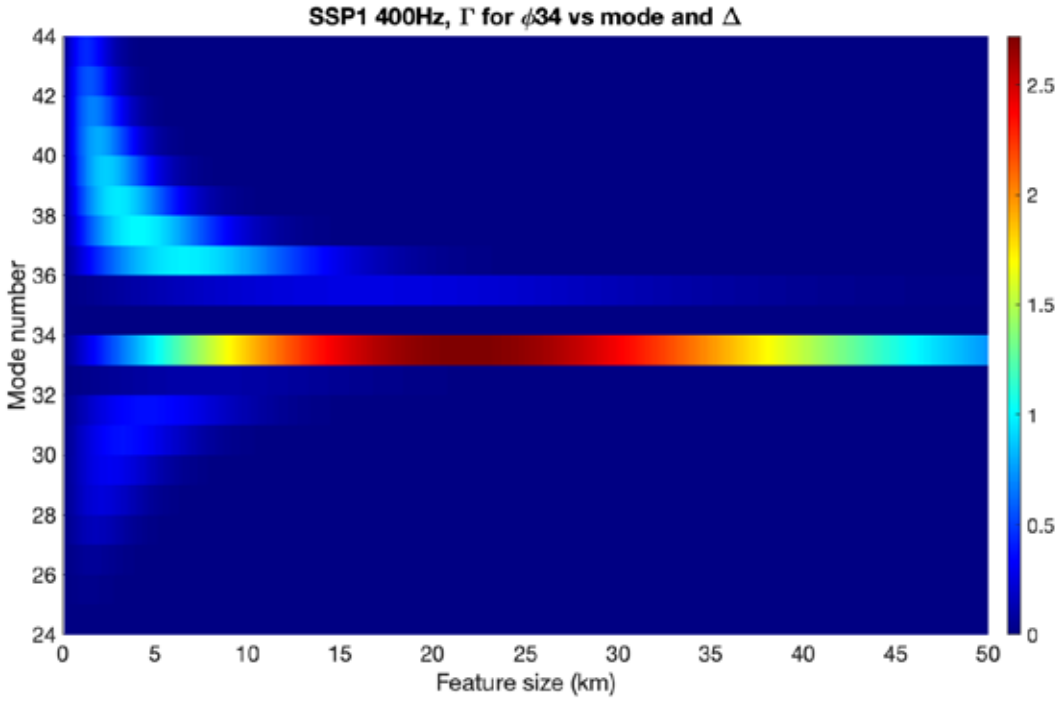

Figure 11. Γ values for the primary trapped ML mode (mode 34) vs. range and mode number. Color bar displays Γ values.

Table 1 lists the maximum Γ_{34n} values and corresponding mode at eight different Δ values as well as the overall maximum Γ_{mn} at that perturbation size. As Δ increases both Γ_{34n} and the overall Γ_{mn} increases. Furthermore, Γ_{mn} is equal to or greater than 1 for all eight feature sizes therefore we expect strong coupling and multiple scattering events even though Γ_{34n} is less than 1 for oceanographic feature sizes of 1 and 3 km.

Table 1. Γ_{mn} values and primary modes of interaction at 400 Hz

Feature Size (km)	Max Γ_{34n}	Strongest Mode of interaction	Max overall Γ_{mn}
1	0.6016	40	1.4211
3	0.9618	38	3.3565
5	1.0051	33	4.0704
7	1.3719	33	5.1434
9	1.7051	33	6.3592
11	1.9975	33	7.4014
13	2.2437	33	8.2485
15	2.4398	33	8.8877

Figure 12 is similar to Figure 11 but for modes 33, 38, and 40 the primary modes of interaction for the one ML mode (mode 34) at the 8 features sizes listed in Table 1.

Figure 12. Γ values for the primary modes of interaction listed in Table 1 (modes 33, 38, 40) vs. range and mode number. Color bar displays Γ values. (Continued on next page.)

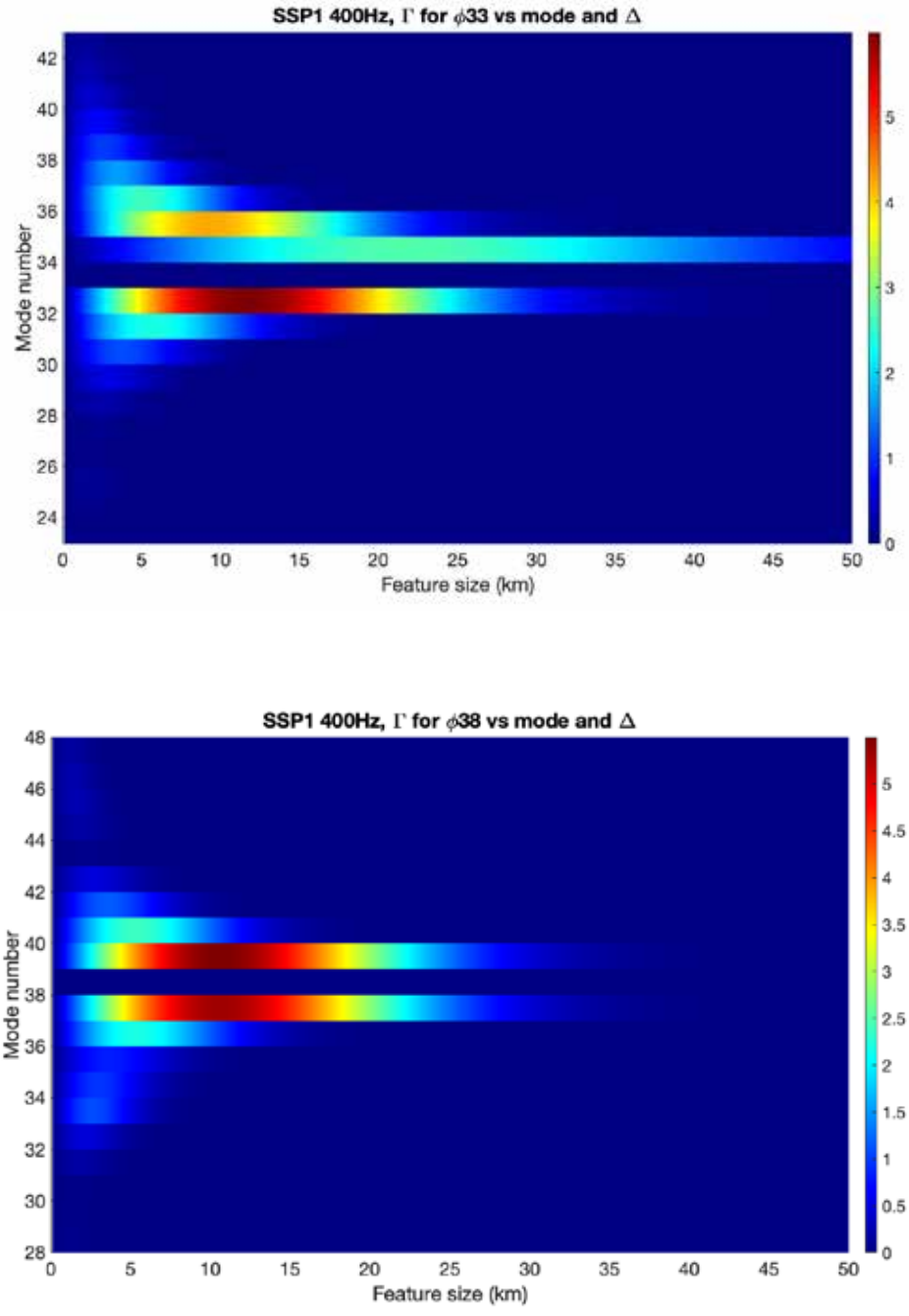

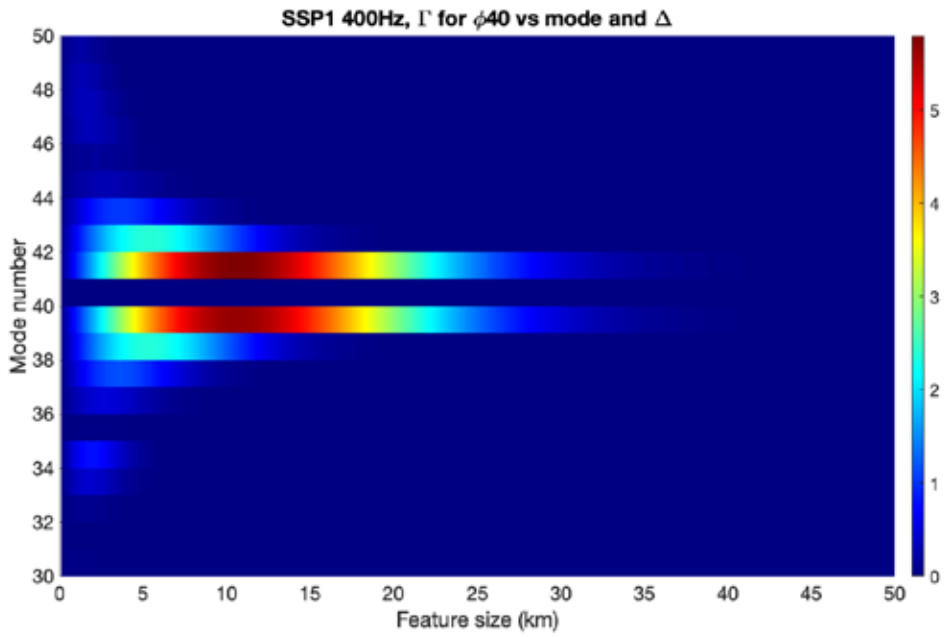

Figure 12, Γ values for the primary modes of interaction, continued from previous page.

We can see that with an overall $\Gamma_{mn} \gg 1$**,** once the ML mode begins to exchange energy a cascading effect takes place where each other mode couples with its preferred mode and so on, reshuffling the energy across many acoustic modes. This is the signature of multiple scattering.

Full physics simulations at 400 Hz: Recall that for the direct simulation we used the eigenvalue method described in Dozier and Tappert (1978b), which provides a numerical solution to Equation 7. Figure 13 shows the mode energy versus range for Δ = 1, 5, 9, 15 km. We set the initial energy of all modes equal to zero with the exception of the primary trapped mode. Recall the existence of the $A_m(0)A_n(0)$ term in Equation. 16, this says if only one mode is excited you need multiple scattering to rearrange the energy. By setting all other initial mode energy to zero we can track how the energy is being redistributed during the interaction with the perturbation through multiple scattering

Figure 13. Mode energy versus range for Δ = 1, 5, 9, 15 km.
(Continued on next page.)

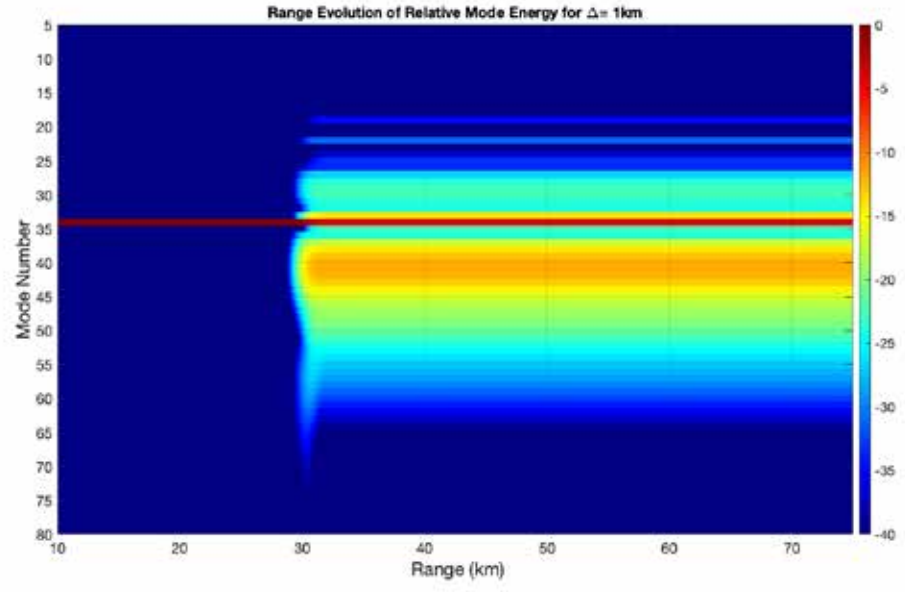

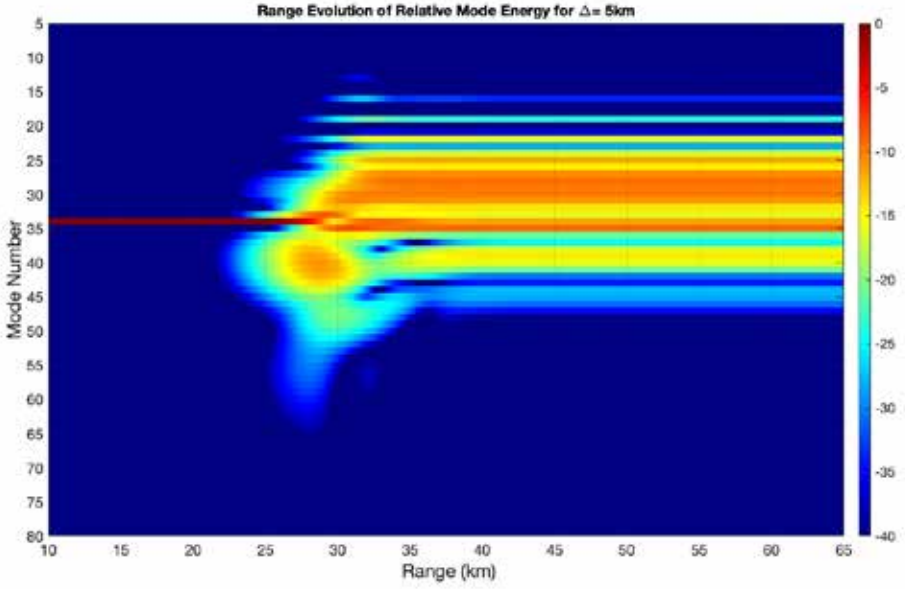

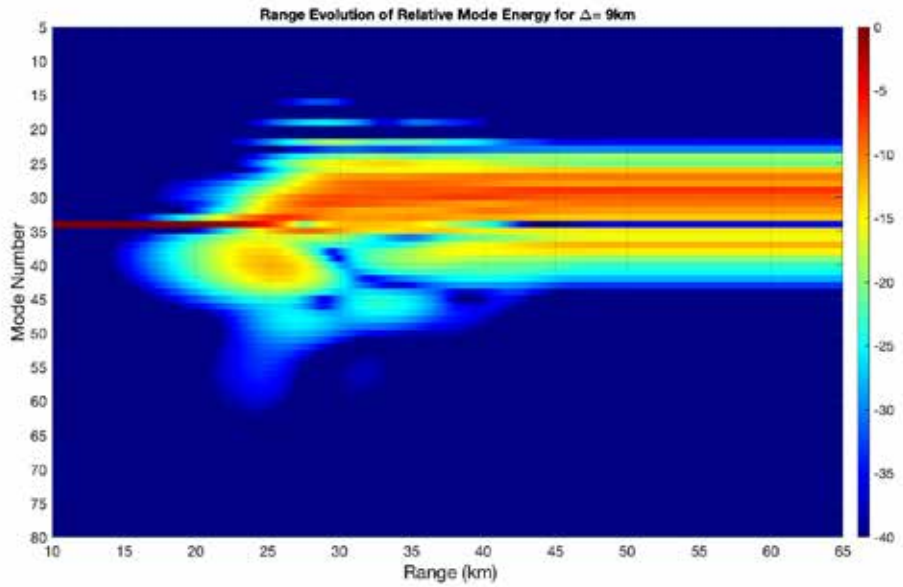

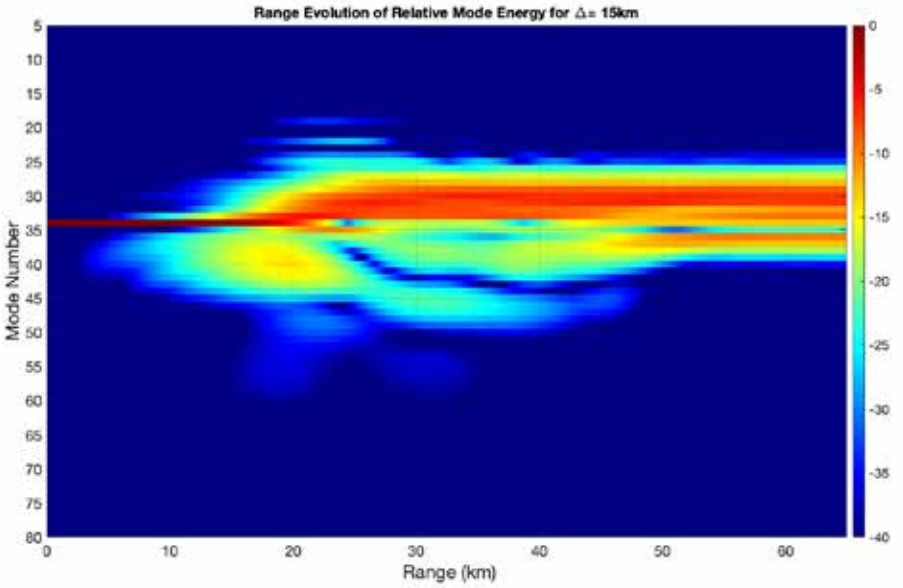

Figure 13, mode energy versus range, continued from previous page.

The results of the full physics simulations match nicely with the analytic model prediction of multiple scattering by depicting a large reshuffling of energy through multiple scattering events for all perturbation sizes with the least complicated pattern being shown

for $\Delta = 1$ km and where Γ is the smallest. In addition, we can see that at 1 km the energy is primarily distributed upward in mode number towards mode 40 but as Δ increases the energy coupling shifts to lower modes centered around mode 33. This shows a strong correlation between the analytic model and the full physics simulations, indicating that Γ_{mn} can successfully be used to identify the shift from single mode scattering to higher order multi-scattering situations as well as identify the primary modes of interaction.

2. Correlation between Increasing Γ_{mn} and TL Variability at 400 Hz

As Δ increases we see increasing Γ_{34n} and increasing overall Γ_{mn} values, thus we expect to see larger TL variability in the MLAD as well. Furthermore, the analytic model identified the primary modes of interaction shown in Figure 11 and Table 1. Mode 34 strongly couples with mode 40, 38, and 33, respectively, as Δ increases. These modes are mix ducted modes having energy throughout the entire water column (Figure 14). Since these primary modes of interaction are all mix ducted modes, we can expect the energy to be scattered out of the MLAD into the deeper water upon interaction creating a shadow zone correlating with the location of the feature.

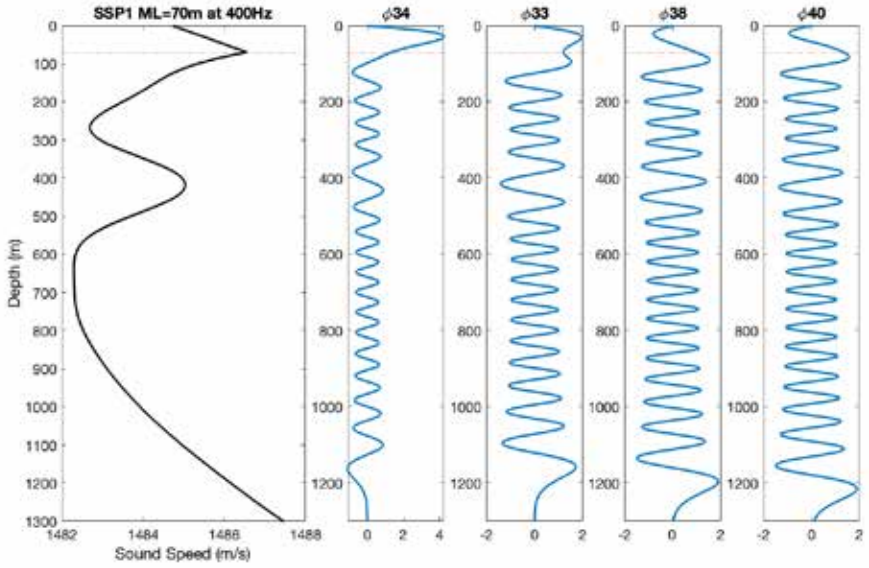

Figure 14. Depiction of primary trapped mode 34 and modes of interaction with depth.

The TL plots shown in Figure 15 agree well with this hypothesis. Here we simulate a 400 Hz source at 40 m depth, and we place the scattering feature at a range of r_0 = 30 km. The MLAD blocking feature becomes quite apparent when Δ = 3 km, that is when Γ_{34n} approaches 1 and the overall $\Gamma_{mn} > 1$. Mode 34 begins to strongly couple with mix ducted modes, and all modes undergo higher order scattering. In addition, the blocking feature becomes more pronounced as Δ increases and likewise Γ_{34n} and overall Γ_{mn} increases. Note also the strong shadow zone that developes behind the blocking feature and extends into the secondary duct.

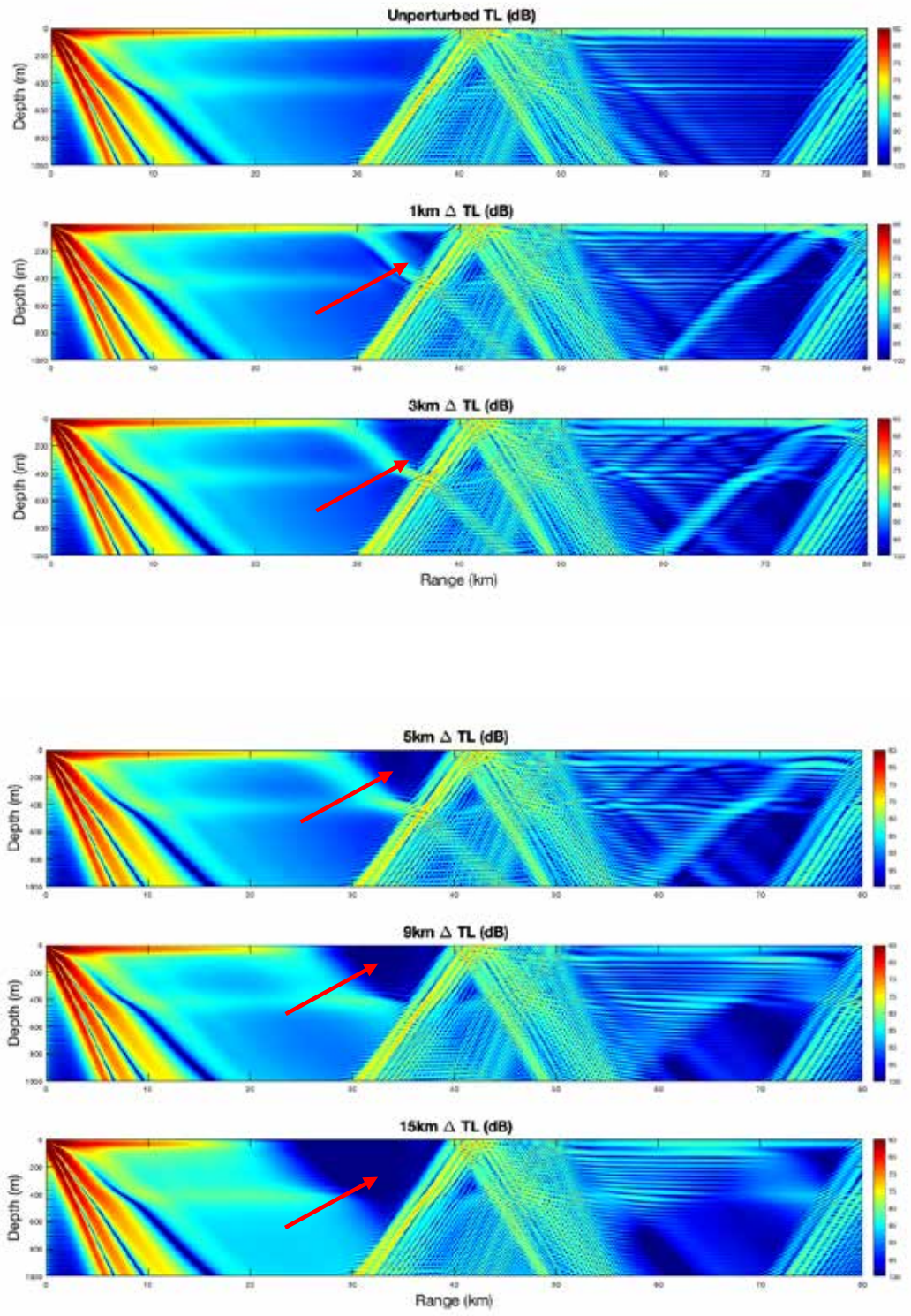

Figure 15. TL plots vs. range for Δ = 1, 3, 5, 9, 15 km.

The ML mode energy loss in dB with range for Δ = 1, 3, 5, 7, 9, 11, 13, 15 km is shown in Figure 16. The energy loss increases as the feature size increases. We also see that for $\Delta = 1\ km$ there is a very smooth transition across the feature indicative of single scattering which corresponds to the lower Γ_{mn} from the analytic model. However, as the feature width increases a notch, circled in Figure 16, appears. The notch is the indication of the beginning of strong multiple scatter events and the reshuffling of energy through the perturbation prior to leveling off on the other side. The appearance of this notch corresponds nicely with increasing Γ_{34n} listed in Table 1 beginning at $\Delta = 3$ km and $\Gamma_{34n} = 0.9618$ and growing larger as Γ_{34n}, overall Γ_{mn}, and Δ increases.

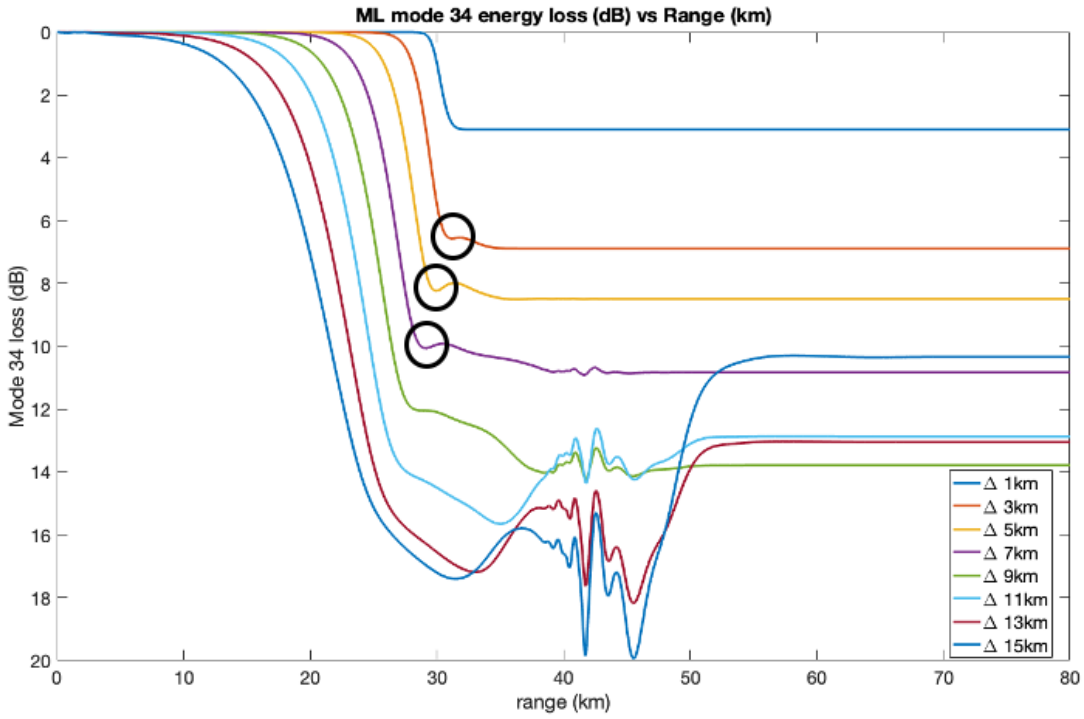

Figure 16. ML mode energy loss in dB with range for Δ = 1, 3, 5, 7, 9, 11, 13, 15 km.

The image on the left in Figure 17 displays mean mode 34 energy loss across the feature as well as the variability in mode 34 energy. The error bar is the standard deviation of the variability around the mean across the feature. The image on the right gives the max

Γ_{mn} for mode 34 as well as modes 33, 38, and 40. The mode 34 energy loss and variability across the feature correlates nicely with the increasing Γ_{mn} values. We have multiple scattering because mode 34 and its primary interacting modes all have $\Gamma > 1$. The tapering off of the mean mode 34 loss seems to be associated with the peaking of Γ for the primary interacting modes. However, the precise details of the mode 34 loss (left panel) will depend on the initial condition.

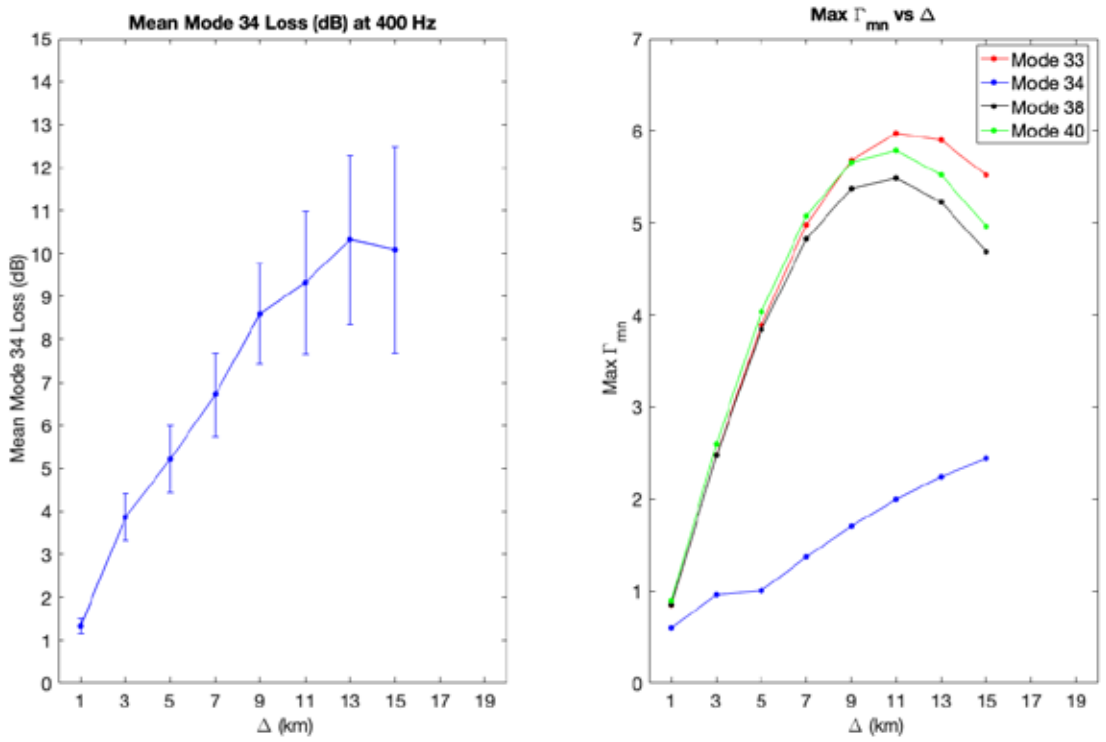

Figure 17. Left image, Mean mode 34 energy loss across the feature as well as the variability in mode energy. Right image, Max Γ_{mn} for mode 34 as well as modes 33, 38, and 40.

B. 1000 HZ SIMULATIONS

1. Correlation between $\Gamma_{mn} \gg 1$ and Multiple Scattering at 1000 Hz

The analytic model: Recall Figure 7 displaying the trapped modes at 1000 Hz. We have three trapped modes at this frequency, modes 70, 83, and 93. Figure 18 shows Γ_{70n},

Γ_{83n}, and Γ_{93n} values for all mode interactions across feature sizes ranging from 100 m to 50 km.

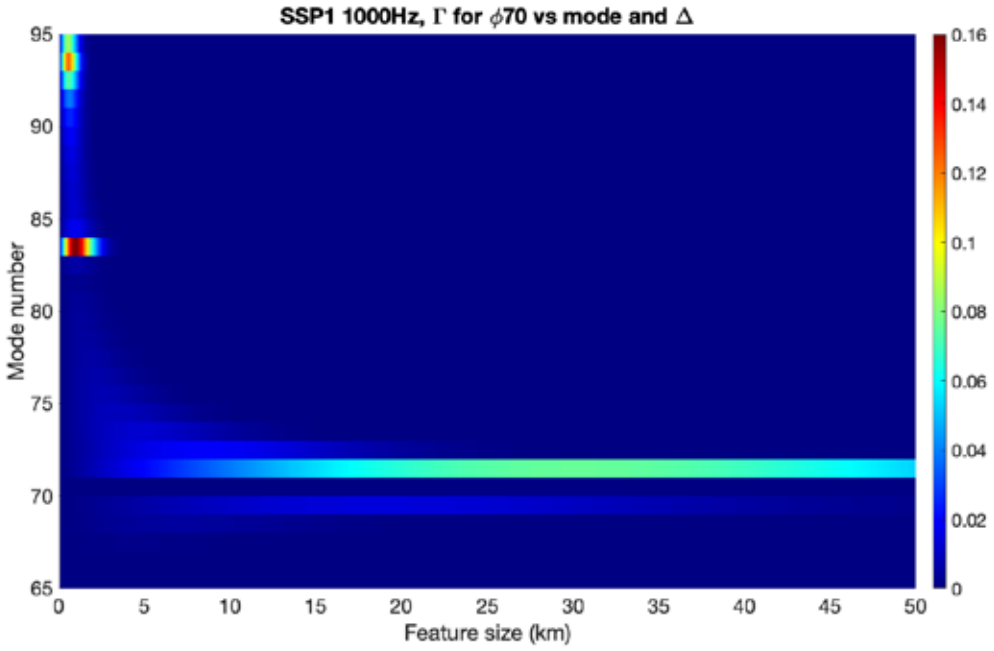

Figure 18. Γ values for the primary trapped ML modes (mode 70, 83, and 93) at 1000Hz vs. range and mode number. Color bar displays Γ values.
(Continued on the next page.)

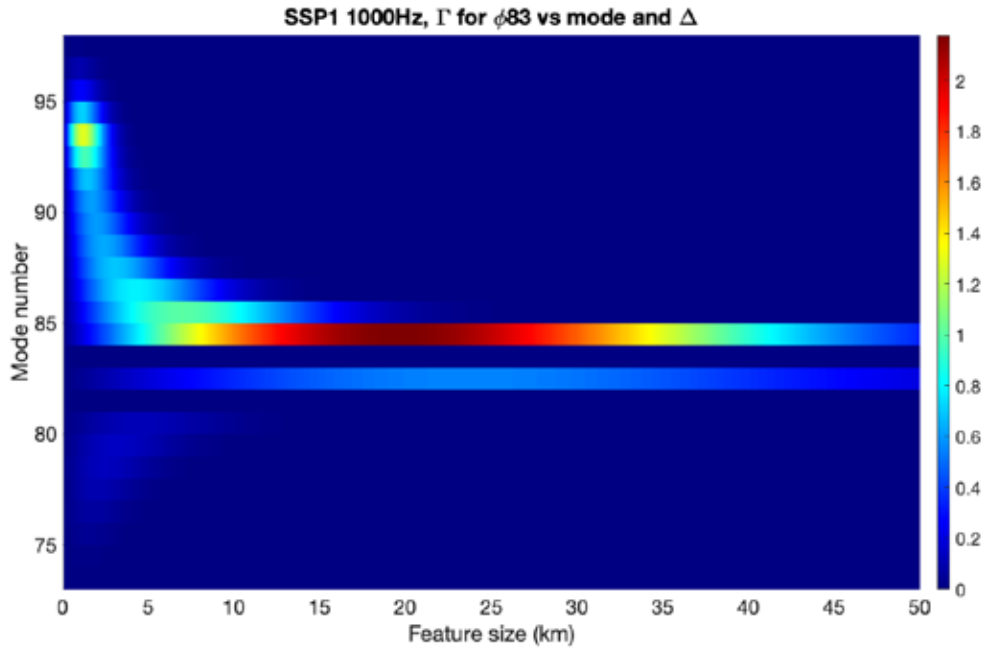

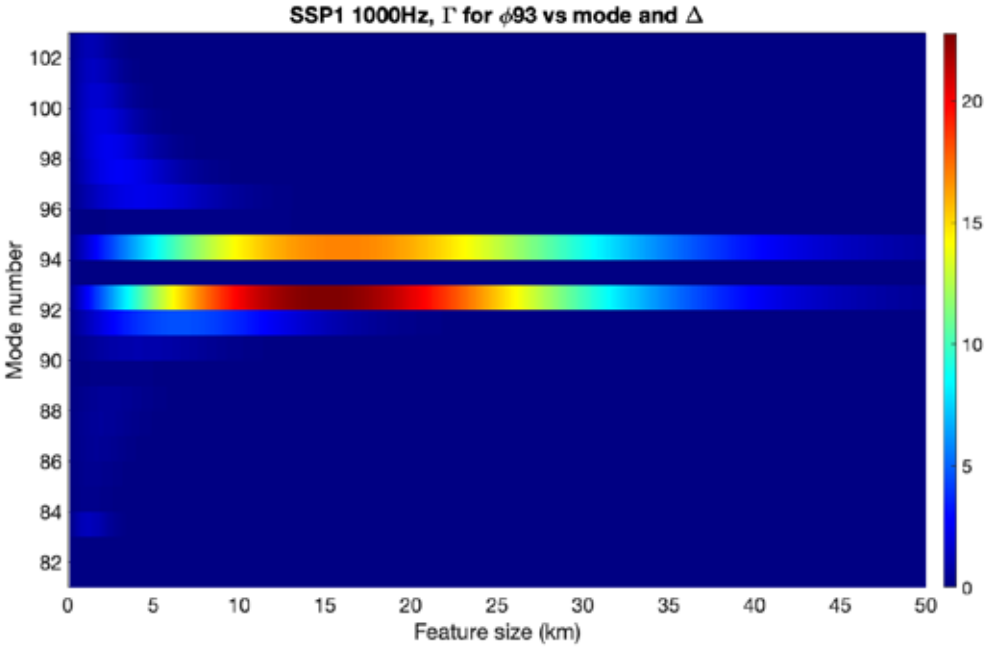

Figure 18, Γ values for the primary trapped ML modes, continued from the previous page.

With Γ_{70n} much less than 1, mode 70 is a very stable mode across all oceanographic feature sizes modeled. This analytic model shows that for $\Delta \leq 1\ km$ mode 70 couples weakly with modes 93 and mode 83. Similarly, mode 83 is coupling with 93 within this Δ range (Γ is a symmetric matrix). Note in Table 2 that Γ_{70n} is always much less than one and Γ_{83n} is far greater than Γ_{70n}, while Γ_{93n} is greater than both other trapped ML modes. Also, the max overall Γ_{mn} is equal to or greater than 1 across all feature sizes. This means there exists strong energy coupling between acoustic modes and reshuffling of mode energy upon interaction with these features.

Table 2. Γ_{mn} values and primary modes of interaction at 1000 Hz

Feature Size (km)	Max Γ_{70n}	Strongest Mode of interaction	Max Γ_{83n}	Strongest Mode of interaction	Max Γ_{93n}	Strongest mode of interaction	Max overall Γ_{mn}
0.5	0.1231	93	0.8379	93	1.2604	92	1.8536
1	0.1595	83	1.2691	93	2.5165	92	3.6263
1.50	0.1170	83	1.1978	93	3.7641	92	5.2480
3	0.0123	71	0.7197	86	7.4141	92	8.7457
5	0.0203	71	0.9221	85	11.9187	92	11.9187
7	0.0281	71	1.2076	84	15.8061	92	15.8061
9	0.0355	71	1.4889	84	18.9057	92	18.9057
11	0.0424	71	1.7268	84	21.1116	92	21.1116
13	0.0488	71	1.9163	84	22.3876	92	22.3876
15	0.0547	71	2.0546	84	22.7638	92	22.7638

Figure 19 shows the Γ_{mn} values for all modes of interaction listed in Table 2. We see very large Γ_{mn} values beginning at much smaller feature sizes ($\Delta \leq 3\ km$) compared to the 400 Hz example. So a key conclusion is that higher frequency is more sensitive to smaller scale features. Similar to 400 Hz, this model is showing that 1000 Hz is in a multiple scattering regime with strong coupling and energy exchange and reshuffling across the features.

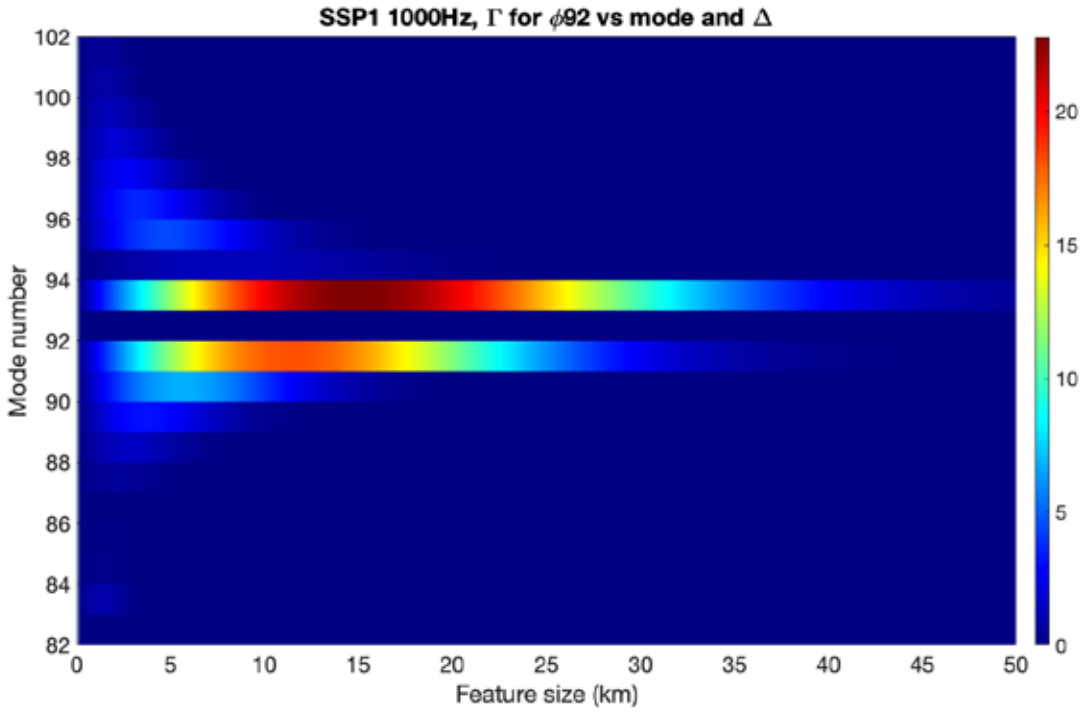

Figure 19. Γ values for the primary modes of interaction listed in Table 2 (modes 92, 86, 85, 84, and 71) vs. range and mode number. Color bar displays Γ values.(Continued on the next page.)

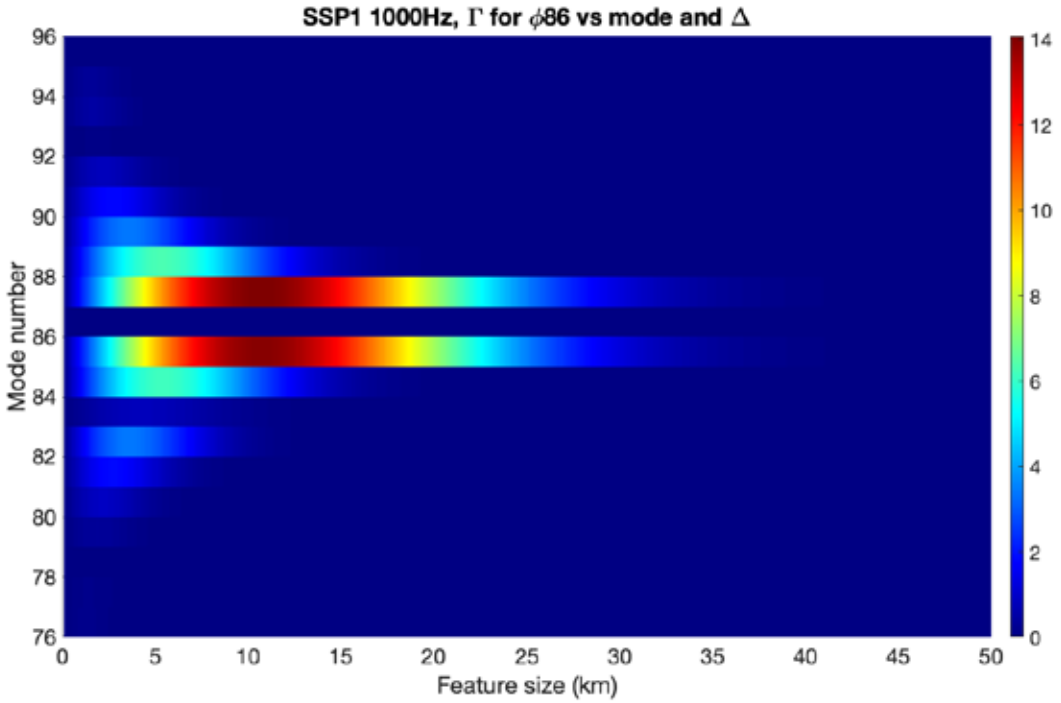
SSP1 1000Hz, Γ for ϕ86 vs mode and Δ
Mode number
Feature size (km)
96
94
92
90
88
86
84
82
80
78
76
0
5
10
15
20
25
30
35
40
45
50
14
12
10
8
6
4
2
0

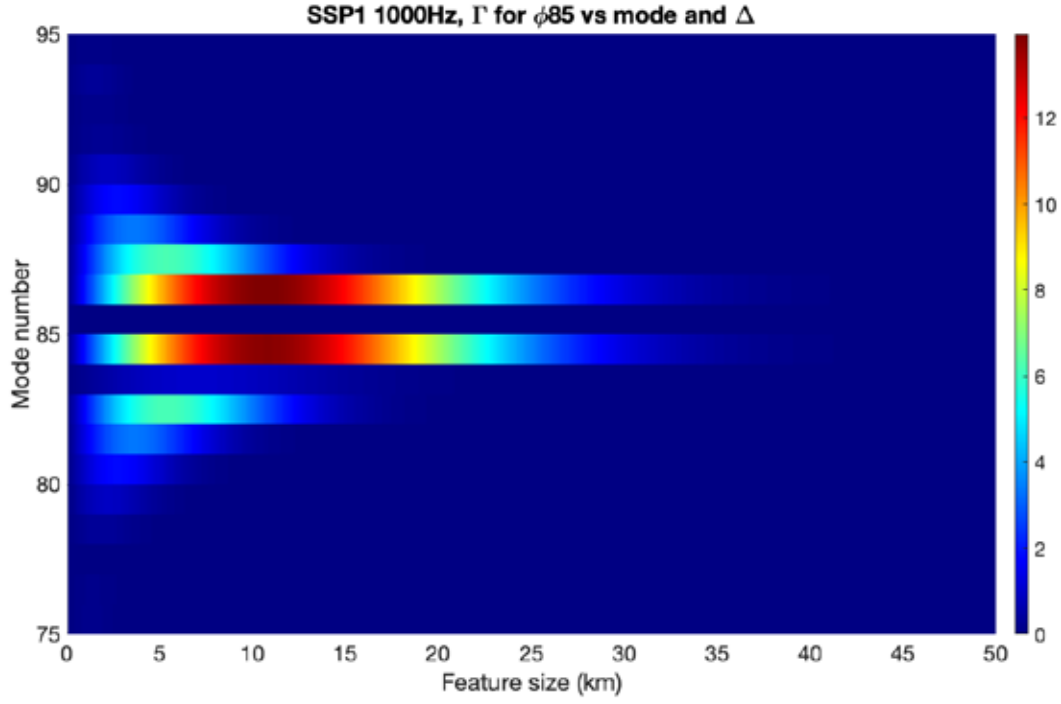
SSP1 1000Hz, Γ for ϕ85 vs mode and Δ
Mode number
Feature size (km)
95
90
85
80
75
0
5
10
15
20
25
30
35
40
45
50
12
10
8
6
4
2
0

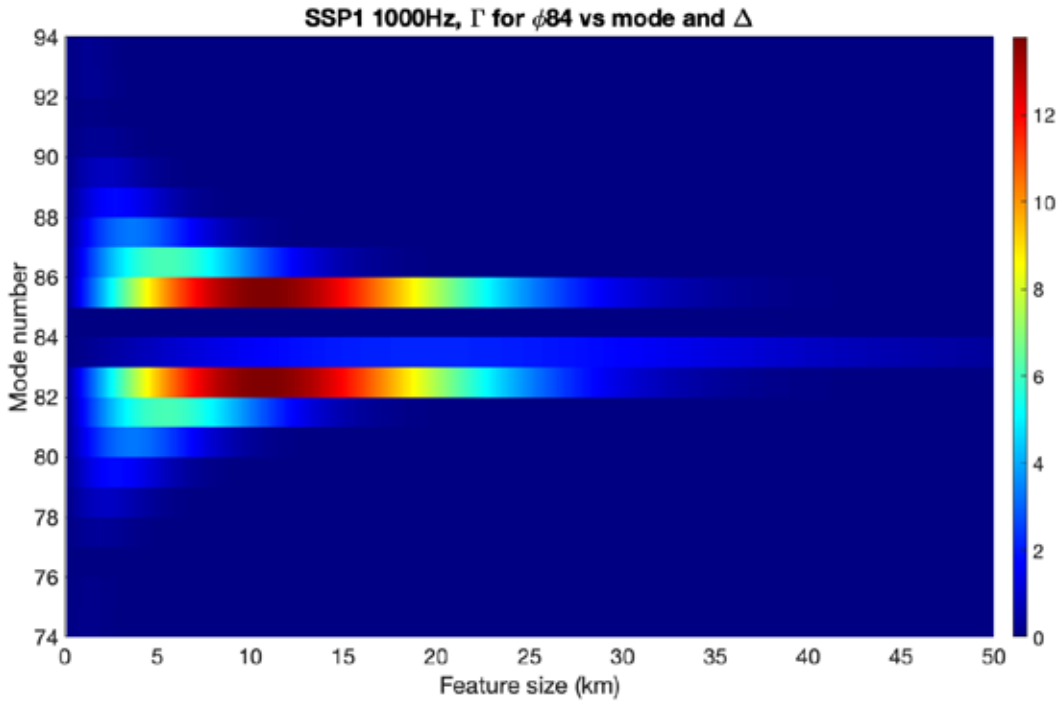

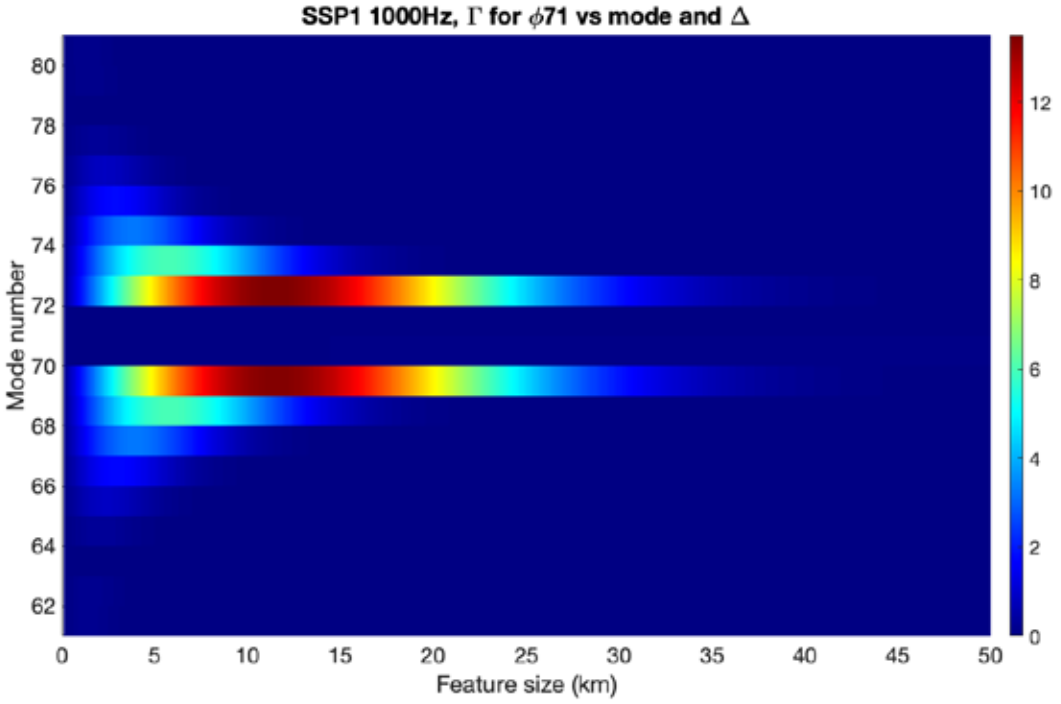

Figure 19, Γ values for the primary modes of interaction, continued from previous pages.

Full physics simulations at 1000 Hz: Figure 20 is analogous to Figure 13 showing the mode energy versus range at various Δ sizes at 1000 Hz. As with Figure 13, the initial energy of all modes has been set to zero with the exception of mode 83, the most interactive of the three trapped modes.

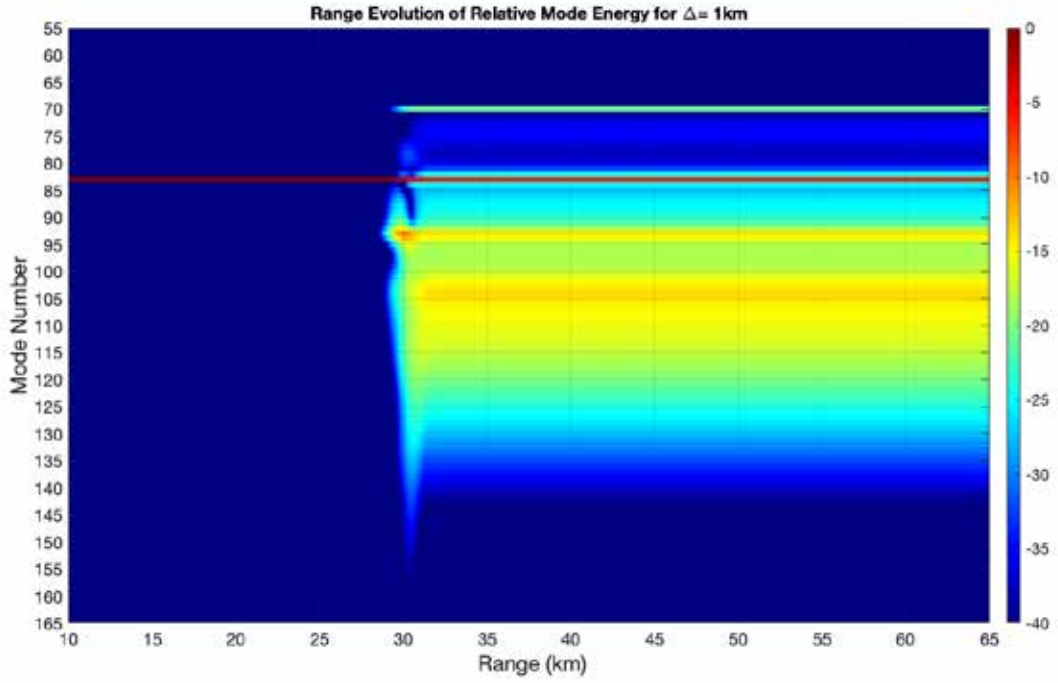

Figure 20. Mode energy versus range at 1000 Hz for Δ = 1, 5, 9, 15 km.
(Continued on the next page.)

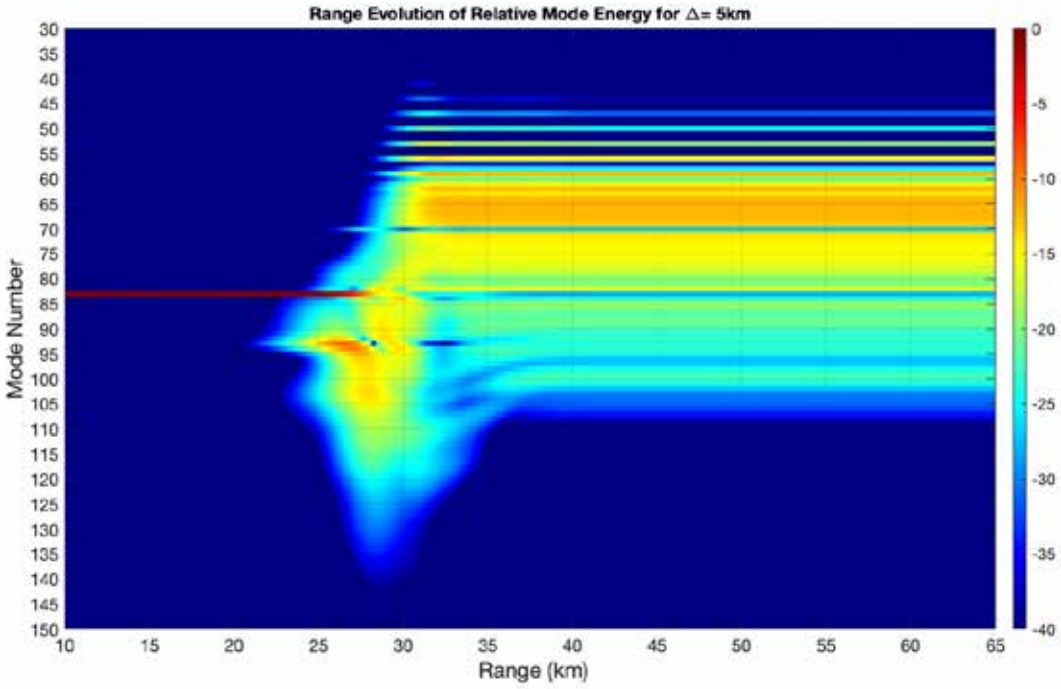
Range Evolution of Relative Mode Energy for Δ= 5km
Mode Number
Range (km)
30 35 40 45 50 55 60 65 70 75 80 85 90 95 100 105 110 115 120 125 130 135 140 145 150
10 15 20 25 30 35 40 45 50 55 60 65
0 -5 -10 -15 -20 -25 -30 -35 -40

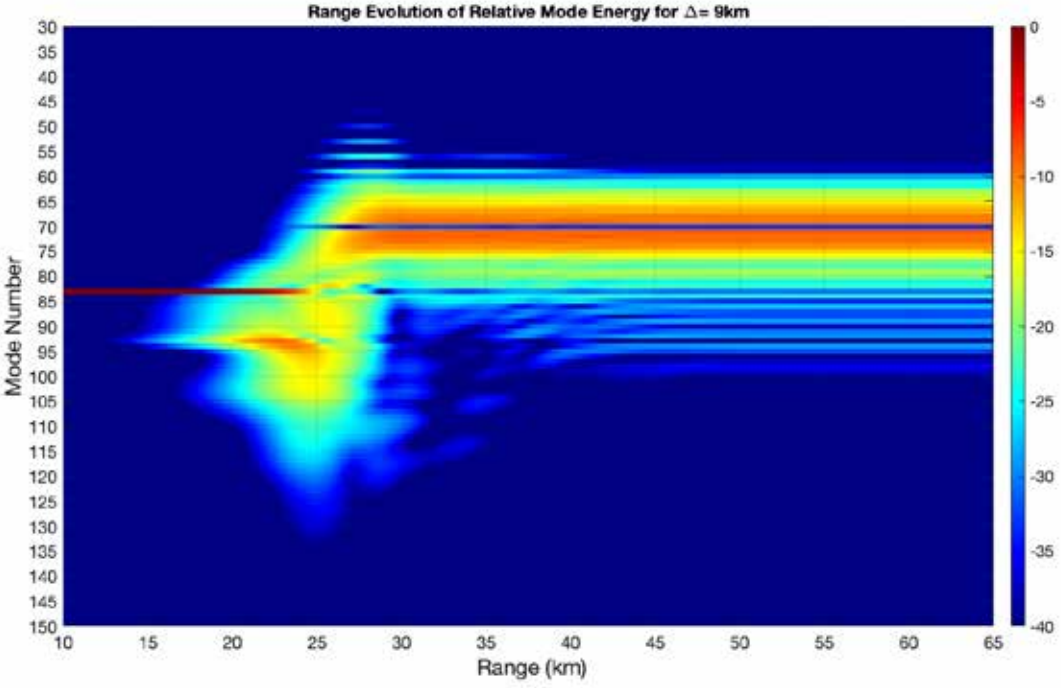
Range Evolution of Relative Mode Energy for Δ= 9km
Mode Number
Range (km)
30 35 40 45 50 55 60 65 70 75 80 85 90 95 100 105 110 115 120 125 130 135 140 145 150
10 15 20 25 30 35 40 45 50 55 60 65
0 -5 -10 -15 -20 -25 -30 -35 -40

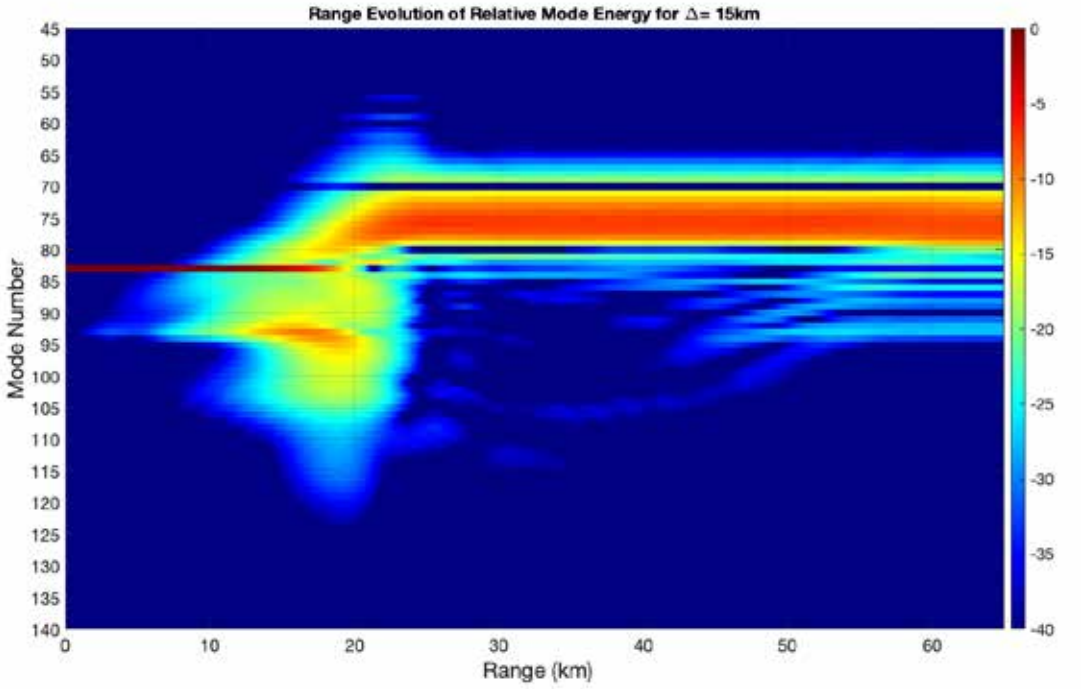

Figure 20, mode energy versus range at 1000 Hz, continued from previous page.

Comparable to the 400 Hz situation, the images in Figure 20 show that these trapped ML modes exchange energy with many other modes through higher order multi-scattering events across all Δ values. This matches nicely with the analytic model which yielded Γ_{mn} values greater than 1 for all feature sizes. This solidifies that Γ_{mn} can successfully be used to identify when acoustic modes shift from single mode scattering to higher order multi-scattering situations.

2. Correlation Between Increasing Γ_{mn} and TL Variability at 1000 Hz

Analogous to the 400 Hz example, we expect to see increased TL variability in the MLAD with increasing overall Γ_{mn} values. Furthermore, this model identified the primary modes of interaction and Figure 21 depicts the coupled modes listed in Table 2. We see that only modes 70, 83, and 93 have significant energy within the duct and all other primary interaction modes are outside the MLAD. Therefore, we can conclude for Δ = 0.5, 1, and 1.5 km most of the acoustic energy will remain in the duct while propagating through the

feature. However, for Δ = 3 km and greater modes 83 and 93 couple with deeper ducted modes and theses perturbations will scatter ducted energy out of the MLAD deeper into the water column. Since mode 70 has $\Gamma_{70n} \ll 1$ and therefore weakly couples we expect to see some amount of the original MLAD energy remain in the duct for all feature sizes. Also, mode 93 strongly couples with mode 92 across all feature lengths. Mode 92 is a mix ducted mode with some energy in the MLAD but significant energy below the duct. Therefore, we can conclude that any energy initially in or transferred to mode 93 will be scattered throughout the water column. Note, due to the complixity at 1000 Hz especially at Δ = 1–3 km, we included a 0.5 km and 1.5 km feature size model in addition to the values used at 400 Hz.

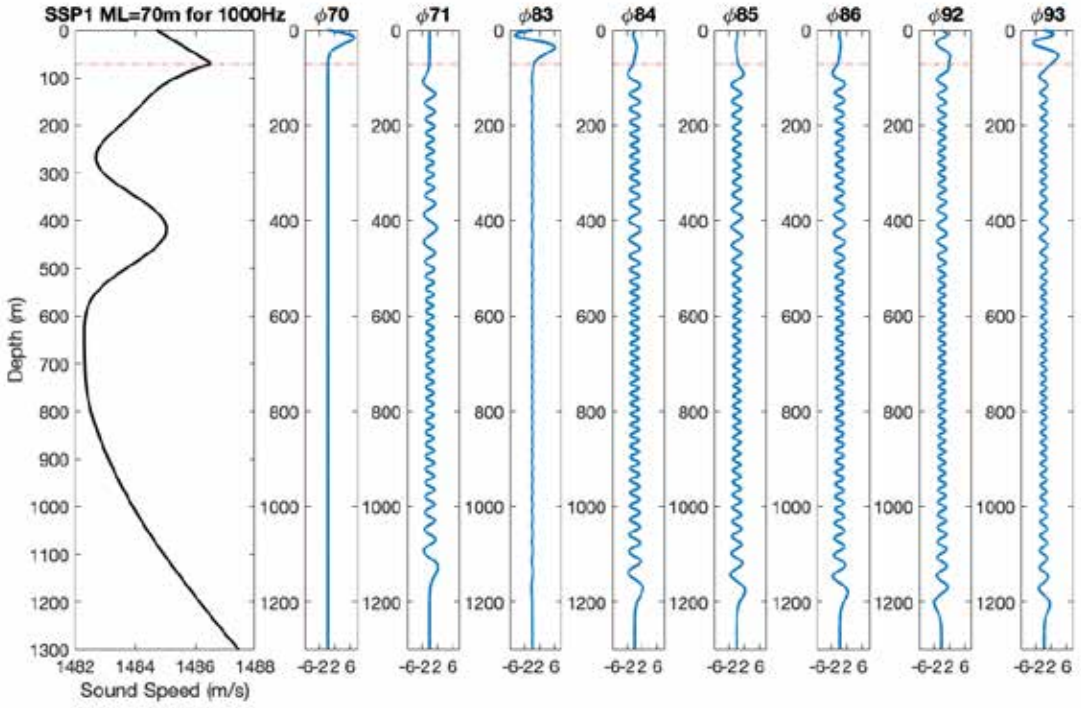

Figure 21. Depiction of primary trapped modes 70 and 83 as well as modes of interaction identified in Table 2 with depth.

Looking at the TL plots in Figure 22 we see that the Γ_{mn} values from the analytic model matches nicely with the full physics simulations. There is a 70% increase in Γ_{83n}

from Δ = 0.5 to Δ = 1.5 km and a blocking feature develops in the 1.5 km TL plot. However, Γ_{83n} decreases 60% to 0.7197 at Δ = 3 km and remains below 1 until Δ = 7 km. We notice that the blocking feature displayed in the 1.5 km TL plots weakens at 3 km and 5 km, but is present again in the 7 km and all larger TL plots which correlates well with growing Γ_{83n}. We also notice that some form of a MLAD remains for all feature sizes. We conclude that this is because mode 70 weakly couples with other modes and retains most of its energy upon interacting with the feature.

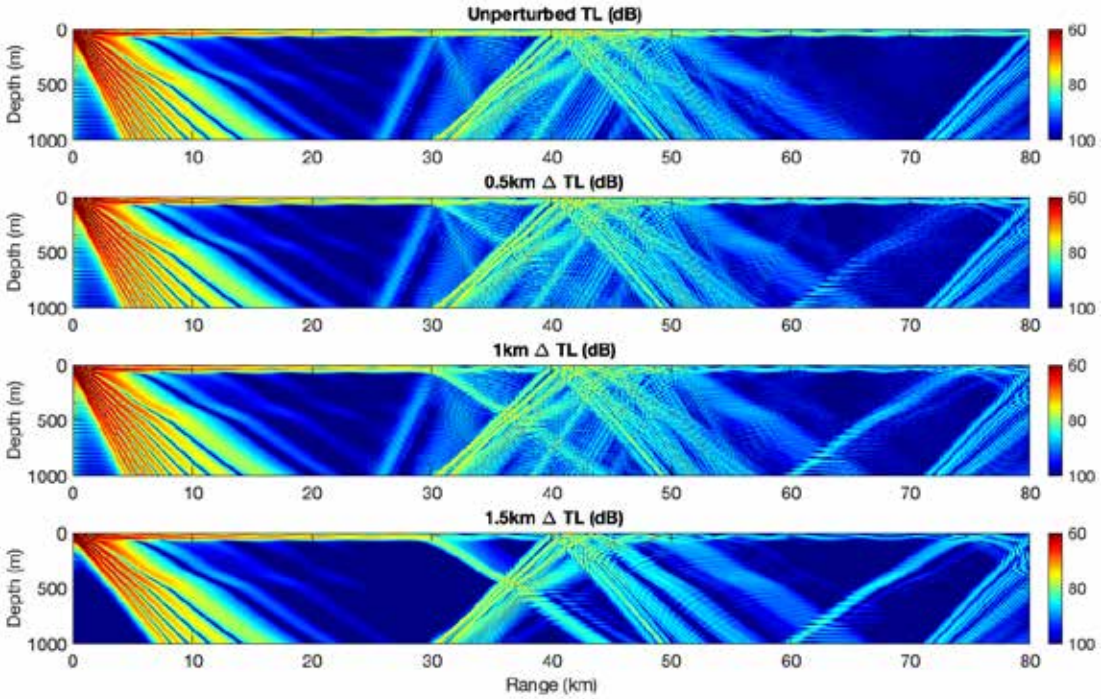

Figure 22. TL plots vs. range for Δ = 0.5, 1, 1.5, 3, 5, 7, 9, 11, 13, 15 km.
(Continued on the next page.)

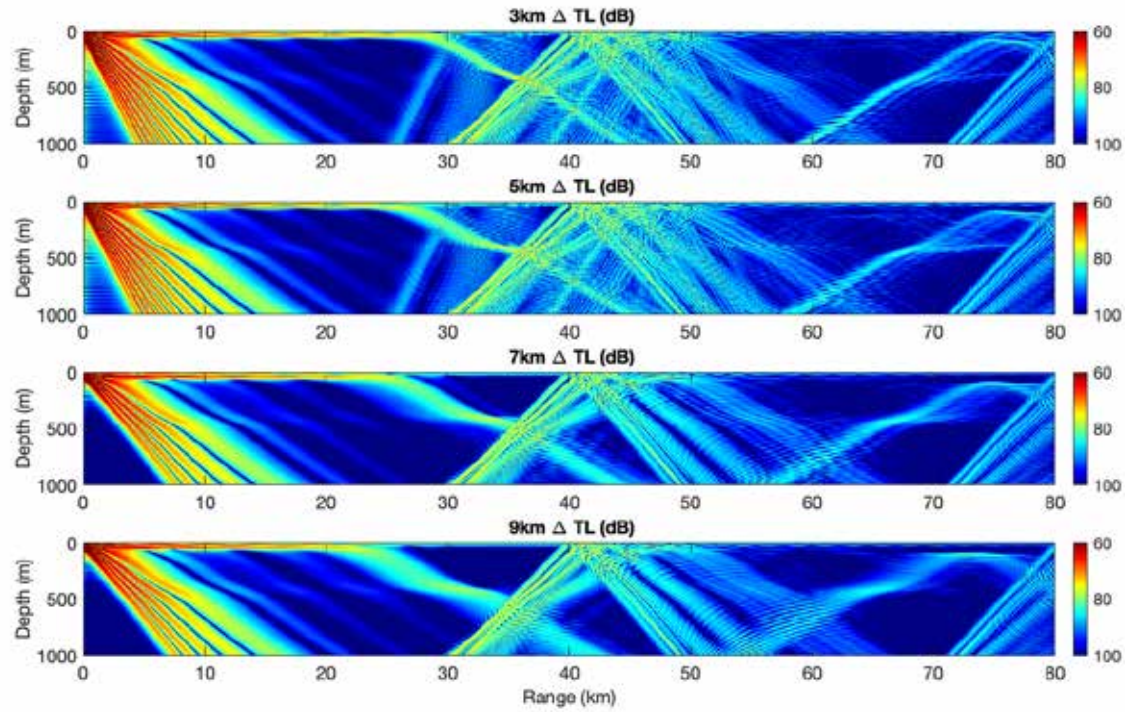

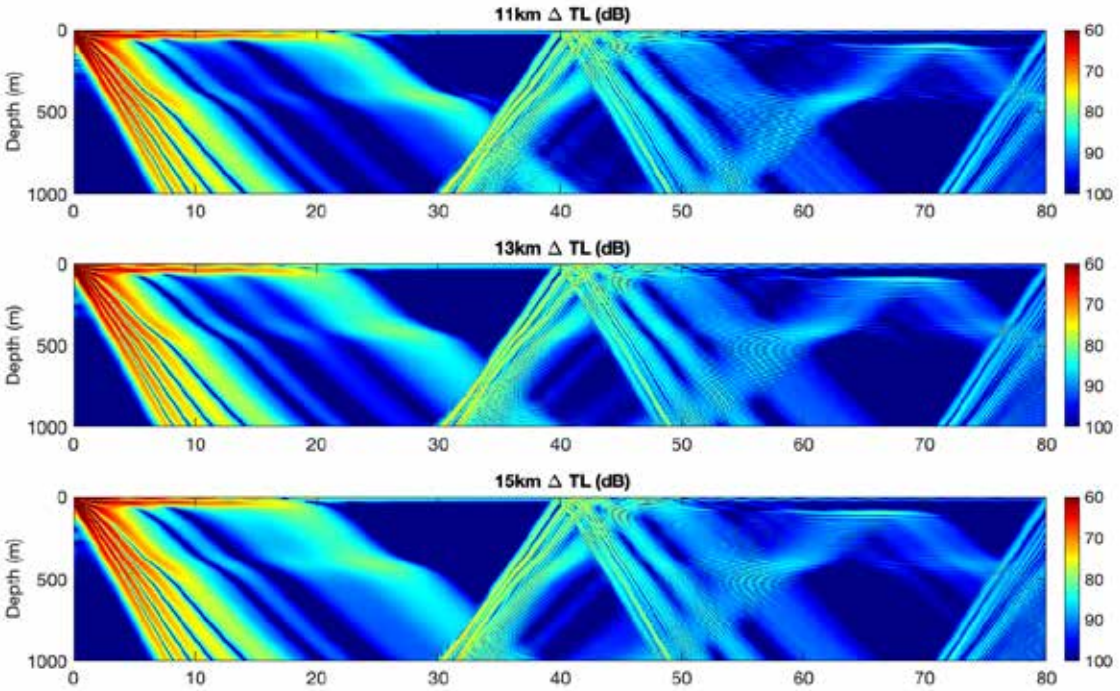

Figure 22, TL plots vs. range, continued from the previous page.

The energy loss of mode 83 vs. range for the various feature sizes, Figure 23, is strongly correlated with the Γ_{83n} and overall Γ_{mn} values from Table 2. As seen with the 400 Hz case, we have a smooth transition across smaller features (0.5 km, 1 km, 1.5 km). However, here we note that Γ_{83n} = 1.2691 and 1.1978 for Δ = 1 and 1.5 km and we still see a smooth transition where at the 400 Hz the smooth transition only existed for Γ_{34n} much less than 1. We also see the presence of the notch developing at a feature size of 3 km even though Γ_{83n}= 0.7197. We believe this is because the overall Γ_{mn}= 8, meaning that the coupling of all other modes is dominating the acoustic structure. We also note that at 1000 Hz we have 3x more energy loss and 3x larger Γ_{mn} values at 15 km than we did at 400 Hz. In addition we see that mode 70 and mode 93 energy loss is much more complex across the feature.

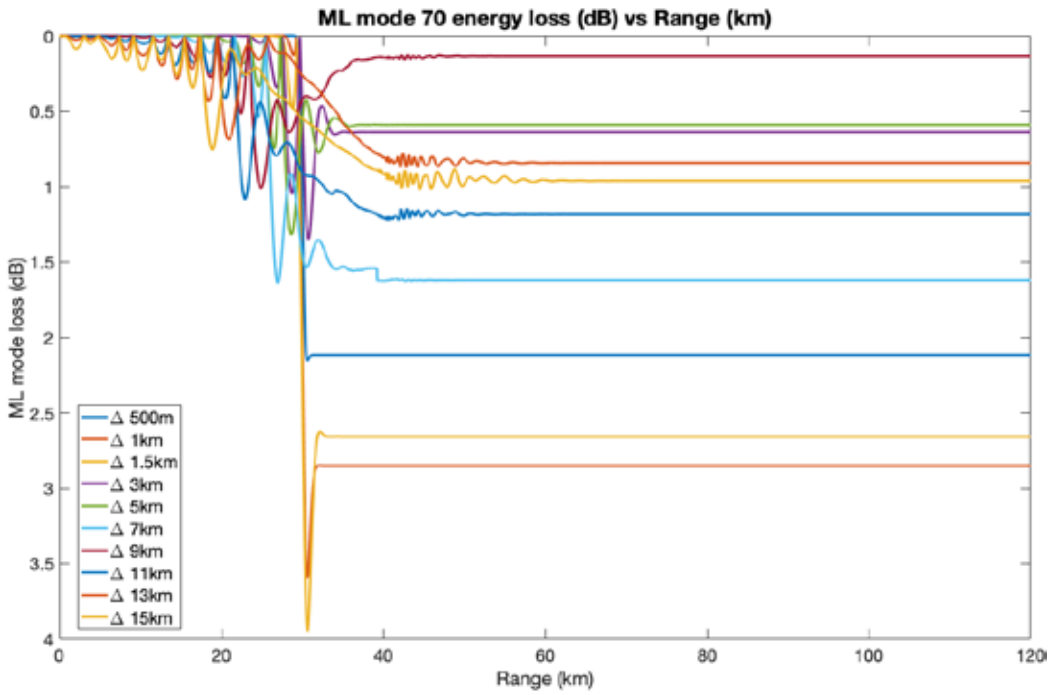

Figure 23. ML mode 70, 83, and 93 energy loss in dB with range for Δ = 0.5, 1, 1.5, 3, 5, 7, 9, 11, 13, 15 km. (Continued on the next page.)

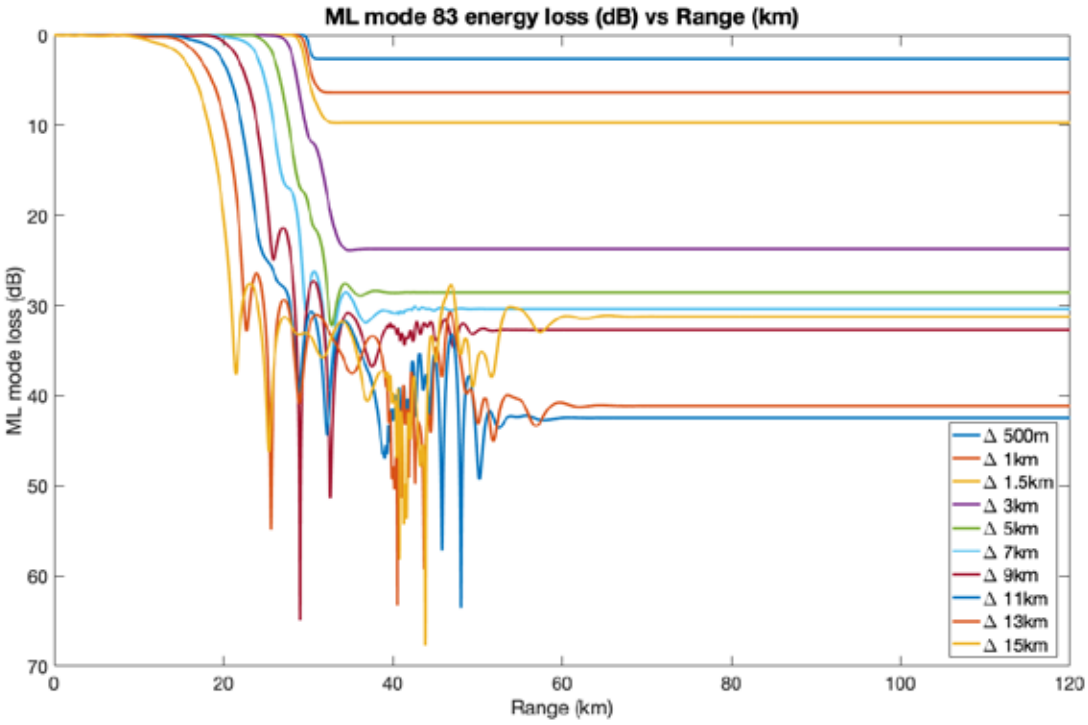

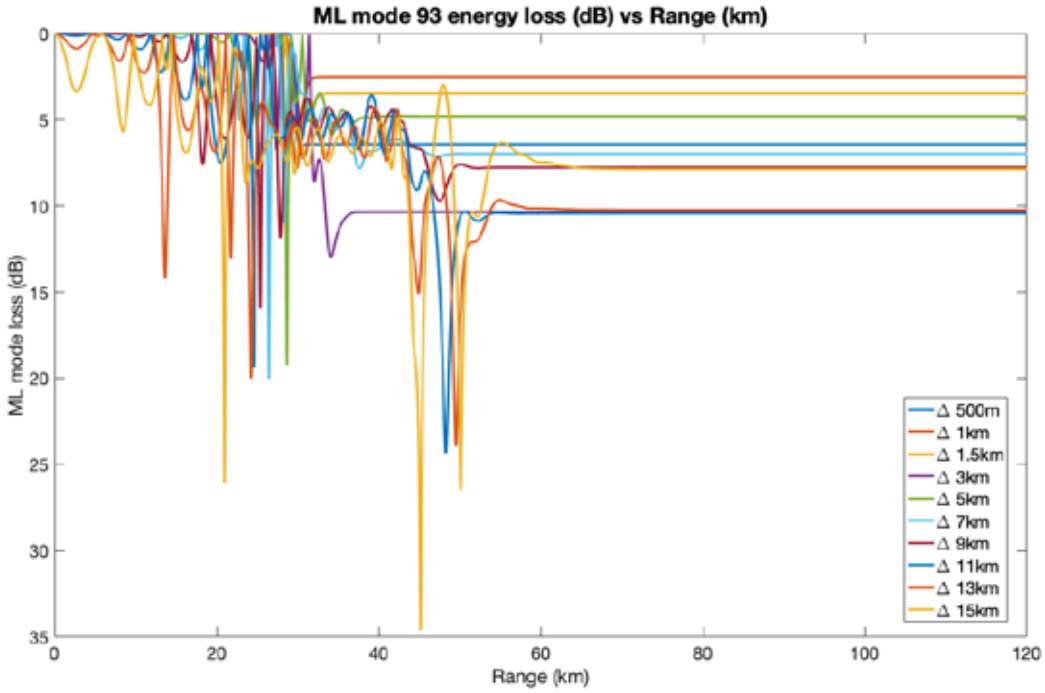

Figure 23, ML mode70, 83, and 93 energy loss in dB with range, continued from previous page.

Lastly, the first image of Figure 24, Figure 25, and Figure 26 displays mean mode energy loss across the feature as well as the variability in mode energy for modes 70, 83, and 93, respectively. The image on the right gives the max Γ_{mn} for those same modes as well as the max Γ_{mn} for the primary modes of interaction listed in Table 2. The mean mode energy loss and variability across the feature correlates nicely with the increasing Γ_{mn} values. Note that mean mode energy loss for mode 70 is less than 2 dB which corresponds to the small Γ_{70n} predicted by this model indicating a very stable mode with weak coupling across the feature. Also, we see that the mean mode energy loss in dB for mode 93 is between -4 and 4. Significantly less than mode 83 indicating that mode 83 is the primary mode of interaction across the feature.

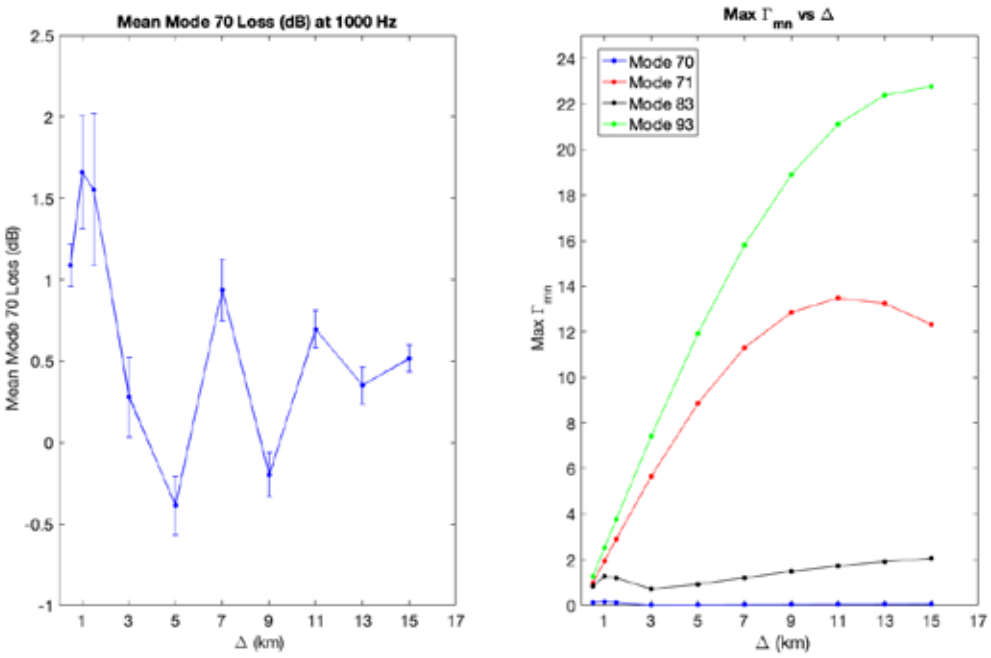

Figure 24. Left image, Mean mode 70 energy loss across the feature as well as the variability in mode energy. Right image, Max Γ_{mn} for mode 70 as well as modes 71, 83, and 93 the primary modes of interaction for mode 70 listed in Table 2.

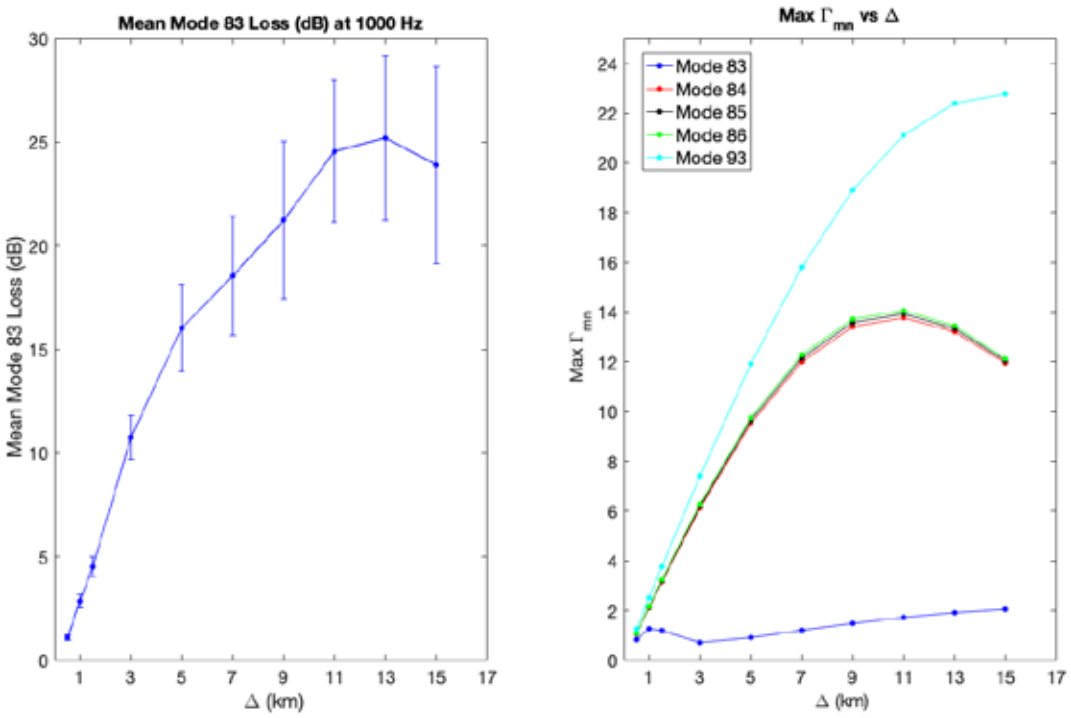

Figure 25. Left image, Mean mode 83 energy loss across the feature as well as the variability in mode energy. Right image, Max Γ_{mn} for mode 83 as well as modes 84, 85, 86, and 93 the primary modes of interaction for mode 83 listed in Table 2.

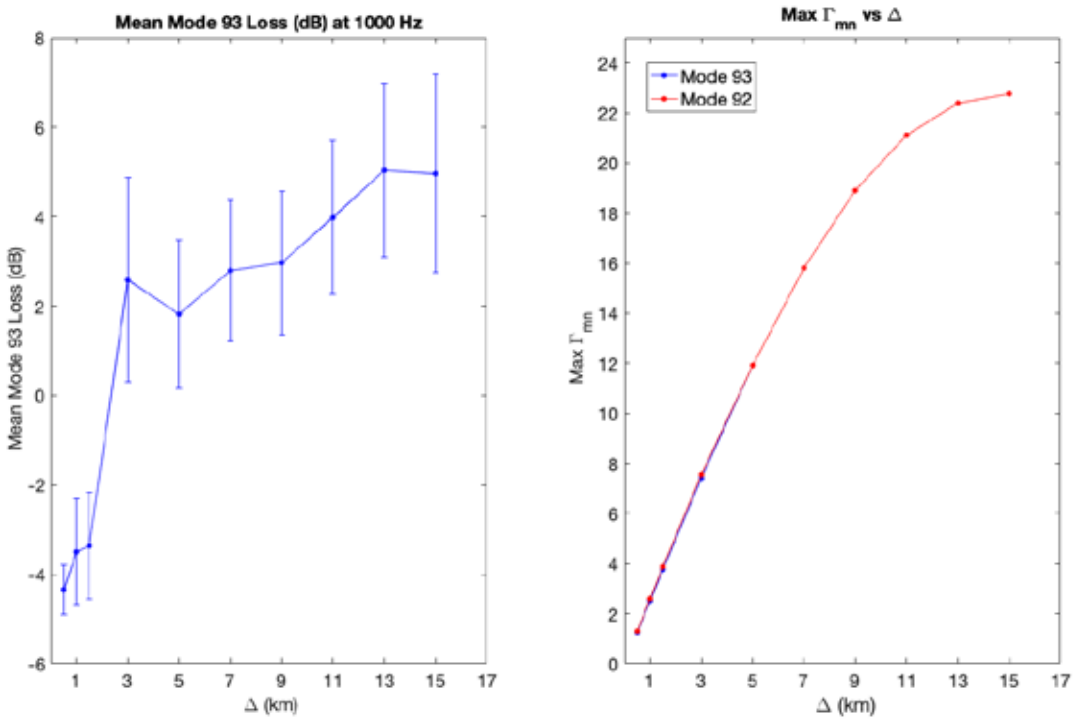

Figure 26. Left image, mean mode 93 energy loss across the feature as well as the variability in mode energy. Right image, max Γ_{mn} for mode 93 and mode 92 the primary mode of interaction for mode 93 listed in Table 2.

IV. CONCLUSION

The goal here was to determine whether:

1. The analytic approach developed for shallow water in Colosi (2008) could be expanded for deeper water with similar results.

2. The single scattering Dyson series approach from Colosi (2008) could provide an understanding of acoustic stability of propagation through perturbations in deeper water environment?

We conclude that the mode energy in Equation 16 derived from Colosi (2008) cannot be accurately applied since the mode coupling in this study was significantly stronger than the shallow water cases examined in the 2008 paper. However, the mode energy equation motivates the definition of Γ_{mn}, the interaction parameter, and these results show strong correlation between Γ_{mn}, multiple scattering events, and TL variability when $\Gamma_{mn} \gg 1$. $\Gamma_{mn} \gg 1$ indicates strong coupling across all modes, higher order scattering, and increased TL variability across the feature. We also showed that Γ_{mn} can be used to identify the primary modes of interaction and by analyzing these primary modes of interaction one can deduce how the oceanographic feature will effect ducted propagation. Furthermore, when Γ_{mn} increases there is an increase in TL variability.

Operationally, the results from this thesis can be used to quickly identify acoustic stability of frequencies of interest based on oceanographic features present in the water space. Current acoustic models require both source and receiver depth information to yield acoustic propagation analysis. Since the target and receiver depths are both varying in time and space this would require running acoustic models for a multitude of source and receiver depths which is very time consuming. Using the interaction parameter, Γ_{mn}, one could quickly identify the primary modes of interaction and quantify acoustic stability without the need for guessing source and receiver depth at every point along the track.

The interaction parameter, Γ_{mn}, could additionally be used to indentify acoustic stability in upcoming water spaces based on typical oceanographic feature sizes of prospective regions. This cabability may allow the user to identify an optimal frequency of

interest for upcoming water spaces. One that is either highly variable or more stable depending on the mission objectives, providing the operator with a weath of knowledge on how acoustic frequencies will behave along the track.

V. FUTURE RESEARCH

The power of the interaction parameter, Γ_{mn}, is by no means fully exhausted with the completion of this thesis. With the dependence of Z_{mn}, Equation 17, on the background SSP and perturbation strength, one could explore different background SSPs and perturbation strengths to see if this Γ_{mn} hypothesis holds true in these water spaces as well.

Also, recall that the interaction parameter is independent of source depth, we chose to put the source depth within the MLAD and focus on a limited number of high initial energy trapped modes expecting the energy to leak out of the duct. However, one could see how well Γ_{mn} provides insight on TL variability when the source is below the duct and energy is scattering from the deeper water into the MLAD.

Furthermore, the most obvious next step would be to run simulations for range of frequencies and perturbation sizes. X_{mn}, Equation 18, approaches zero at both extremely small and large Δ and both Z_{mn} and X_{mn} are frequency dependent in the structure of the acoustic modes, φ_m, as well as the beat wavenumber, k_{mn}. It would be enlightening to see how Γ_{mn} performs under those conditions.

Finally, one could explore background profiles that support higher numbers of trapped modes to decipher which modes are exchanging energy causing the TL variability and compare that to the predictions from Γ_{mn}. Recall that the original SSP1 used in this research lacked a MLAD but had a very strong SSC which supported many modes, Figure 9. This was too many modes to disentangle when trying to understand the core physics of the interaction but now with the interaction parameter, Γ_{mn}, somewhat understood it may be possible to disentangle larger mode scenarios.

THIS PAGE INTENTIONALLY LEFT BLANK

LIST OF REFERENCES

Baxter, L., and M. H. Orr, 1982: Fluctuations in sound transmission through internal waves associated with the thermocline: A computer model for acoustic transmission through sound velocity fields calculated from thermistor, CDT, XBT, and acoustic backscattering. *The Journal of the Acoustical Society of America*, **71**, 61–66.

Colosi, J, and Rudnick, D. L. (2020): Observations of upper ocean sound-speed structures in the North Pacific and their effects on long-range acoustic propagation at low and mid-frequencies. *The Journal of the Acoustical Society of America*. **148(4)**, 2040–2060.

Colosi, J. A., 2016: *Sound Propagation Through the Stochastic Ocean.* Cambridge University Press, 420 pp.

Colosi, J. A., 2008: Acoustic mode coupling induced by shallow water nonlinear internal waves: Sensitivity to environmental conditions and space-time scales of internal waves. *The Journal of the Acoustical Society of America*, **124(3)**, 1452–1464.

Dozier, L. B.,1983: A coupled model for spatial coherence of bottom-interacting energy. Proceedings of the Stochastic Modeling Workshop, edited by Spofford, C.W., and J.M. Haynes

Dozier, L. B., and F. D. Tappert, 1978a: Statistics of normal mode amplitudes in a random ocean. I. Theory. *The Journal of the Acoustical Society of America*, **63(2)**, 353–365.

Dozier, L. B., and F. D. Tappert, 1978b: Statistics of normal mode amplitudes in a random ocean. II. Computations. *The Journal of the Acoustical Society of America*, **64**, 353–365.

Finette, S., M. H. Orr, A. Turgut, J. R. Apel, M. Badiey, C. Chiu, R. H. Headrick, J. N. Kemp, J. F. Lynch, A. E. Newhall, K. von der Heydt, B. Pasewark, S. N. Wolf, and D. Tielbuerger, 2000: Acoustic field variability induced by time evolving internal wave fields. *The Journal of the Acoustical Society of America*, **108(3)**, 957–972.

Flatte, S. M., R. Dashen, W. Munk, K. Watson, and F. Zachariasen, 1979: *Sound Transmission Through a Fluctuating Ocean*, Cambridge University Press, 299 pp.

Naval Oceanographic Office, 1986: *Fleet Oceanographic and Acoustic Reference Manual*, Reference Publication.

Presisig, J. C., and T. F. Duda, 1997: Coupled acoustic mode propagation through continental shelf internal nonlinear waves, IEE J. Ocean. Eng. **22**, 256–269.

Rainville, L., and Coauthors, 2019: AR35-03 Cruise report: Near-Inertial Shear and Kinetic Energy in the North Atlantic experiment

Sakurai, J. J., 1985: *Modern Quantum Mechanics*. Addison-Westley, 548 pp.

Tielbuerger, D., S. Finette, and S. Wolf, 1997: Acoustic propagation through an internal wave field in a shallow water waveguide. *The Journal of the Acoustical Society of America*, **101(2)**, 789–808.

Urick, R. J., 1983: *Principles of Underwater Sound*. Peninsula Publishing, 423 pp.

Yang, T. C., 2014: Acoustic mode coupling induced by nonlinear internal waves: Evaluation of the mode coupling matrices and applications. *The Journal of the Acoustical Society of America*, **135(2)**, 610–625.

Zhou, J., X. Zhang, and P. H. Rogers, 1991: Resonant interaction of sound wave with internal solitons in the coastal zone. The *Journal of the Acoustical Society of America*, **90(4)**, 2042–2054.

INITIAL DISTRIBUTION LIST

1. Defense Technical Information Center
   Ft. Belvoir, Virginia

2. Dudley Knox Library
   Naval Postgraduate School
   Monterey, California